Optimal Signal Recovery for Pulsed Balanced Detection

by

Yannick Alan de Icaza Astiz

submitted for the degree of
Doctor of Philosophy

Supervisor: Morgan W. Mitchell

Universidad Politécnica de Cataluña

Instituto de Ciencias Fotónicas

Barcelona, September 2014

Para mis padres y mis hermanos

Para Anaid

Prefacio

Hace años me di cuenta que quería hacer ciencia, dado que siempre me ha gustado cuestionar la manera en cómo se hacen las cosas, entender y descubrir por qué se hacen y al final diseñar nuevas maneras de hacer las mismas. Un día me di cuenta que los pensamientos anteriores al mismo tiempo se pueden clasificar desde un punto de vista filosófico como pensamientos subversivos o revolucionarios. Y por mis años de estudio de la historia, los pensamientos subversivos y revolucionarios siempre son difíciles de asimilar y en muchas ocasiones llevan a conflictos sociales. Así que por lo mismo, en el momento tienes una gran idea que vaya a revolucionar alguna causa, sin lugar a dudas te espera un gran camino por recorrer, no solo para implementar la idea, sino para implantarla y hacerla que se acepte.

Durante mi doctorado en el Instituto de Ciencias Fotónicas (ICFO), aprendí mucha tecnología láser y óptica, además de que aprendí el marco del método científico en la sociedad. El científico tiene que ser un revolucionario por naturaleza, así que aún después de descubrir, entender o desarrollar algo, todavía le queda la mitad del camino por recorrer. Tiene que explicar, demostrar y probar para que al final la sociedad acepte sus ideas.

Abstract

To measure quantum features in a classical world constrains us to extend the classical technology to the limit, inventing and discovering new schemes to use the classical devices, while reducing and filtering the sources of noise. Balanced detectors, e.g. when measuring a low-noise laser, have become an exceptional tool to attain the shot-noise level, i.e., the standard quantum limit for measuring light. To detect light pulses at this level requires to decreasing and also to filtering all other sources of noise, namely electronic and technical noise.

The aim of this work is to provide a new tool for filtering technical and electronic noises present in the pulses of light. It is especially relevant for signal processing methods in quantum optics experiments, as a means to achieve shot-noise level and reduce strong technical noise by means of a pattern function. We thus present the theoretical model for the pattern-function filtering, starting with a theoretical model of a balanced detector. Next, we indicate how to recover the signal from the output of the balanced detector and a noise model is proposed for the sources of noise and the conditions that should satisfy the filtering algorithm. Finally, the problem is solved and the pattern function is obtained, the one which solves the problem of filtering technical and electronic noises.

Once the pattern function is obtained, we design an experimental setup to test and demonstrate this model-based technique. To accomplish this, we produce pulses of light using acousto-optics modulators, such light pulses are precisely characterized together with the detection system. The data are then analyzed using an oscilloscope which gathers all data in the time domain. The frequency-domain repre-

sentation is calculated using mathematical functions. In this way, it is proved that our detector is shot-noise limited for continuous-wave light. Next, it is shown how the technical noise is produced in a controlled manner, and how to gather the necessary information for calculating the pattern function. Finally, the shot-noise-limited detection with pulses without technical noise introduced is shown first, and next, an experimental demonstration where 10 dB of technical noise is then filtered using the pattern function.

The final part of this research is focused on the optimal signal recovery for pulsed polarimetry. We recall the Stokes parameters and how to estimate the polarization state from a signal. Next, we introduce a widely used signal processing technique, the Wiener filter. For the final step, we show how to retrieve, under the best conditions, the polarization-rotation angle with a signal that has 10 dB of technical noise. Obtaining that our technique outperforms the Wiener estimator and at the same time obtaining the standard quantum limit for phase/angle estimation. Because of the correlation between pulsed polarimetry and magnetic estimation using magnetic-atomic ensembles via Faraday effect, this pattern-function filtering technique can be readily used for probing magnetic-atomic ensembles in environments with strong technical noise.

Resumen

Medir las características cuánticas en un mundo clásico no solo requiere llevar al límite la tecnología clásica, sino también, inventar y descubrir nuevos esquemas para utilizar los dispositivos clásicos, reduciendo y filtrando las fuentes de ruido. Los detectores balanceados, cuando miden un láser de bajo ruido, se han convertido en una herramienta excepcional para alcanzar el nivel del ruido de disparo, que es el límite estándar clásico para medir la luz. Detectar pulsos de luz al nivel de ruido de disparo requiere reducir y filtrar todas las otras fuentes de ruido, es decir, el ruido electrónico y el técnico.

El objetivo de este trabajo es crear una nueva herramienta para filtrar ruido tanto técnico como electrónico de pulsos de luz, que es especialmente relevante para los métodos de procesamiento de señales en los experimentos de óptica cuántica, como una manera de alcanzar el nivel de ruido de disparo y reducir fuertemente el ruido técnico por medio una función patrón. Presentamos, por lo tanto, el modelo teórico para el filtrado por una función patrón. Primeramente damos el modelo teórico de un detector balanceado, luego exponemos cómo se recupera la señal de la salida del detector balanceado. A continuación proponemos un modelo para las fuentes de ruido y las condiciones que debe satisfacer el algoritmo de filtrado. Finalmente, se resuelve el problema y se obtiene la función patrón que nos permite filtrar los ruidos técnico y electronico.

Una vez que la función patrón se puede calcular, diseñamos un montaje experimental para probar y demostrar esta técnica basada en un modelo. Para tal propósito, producimos pulsos de luz usando moduladores acusto-ópticos que producen pulsos de luz que están

precisamente caracterizados, junto con el sistema de detección. Los datos se analizan a continuación con un osciloscopio, reuniendo todos los datos en el dominio del tiempo. La representación del dominio de la frequencia se calcula utilizando funciones matemáticas. De esta manera, se prueba que nuestro detector está limitado por el ruido de disparo para luz continua. Después, se muestra cómo se produce el ruido técnico de manera controlada, y cómo se reune la información necesaria para calcular la función patrón. Finalmente, se muestra la detección limitada por el ruido de disparo para pulsos sin ruido técnico introducido primero, y luego, se hace una demostranción experimental con 10 dB de ruido técnico, que se filtra a continuación usando la función patrón.

La parte final de esta investigación está enfocada a la recuperación óptima de la señal para polarimetría pulsada. Recordamos los parámetros de Stokes y cómo estimar el estado de polarización de una señal. Luego, introducimos el filtro de Wiener, que es una técnica ampliamente usada en el procesamiento de señales. Para el paso final, mostramos cómo se recupera, bajo las mejores condiciones, el ángulo de rotación de polarización con una señal que tiene 10 dB de ruido técnico. Obteniendo el límite estándar cuántico para la estimación fase/ángulo y superando así el estimador de Wiener. Debido a la correlación entre polarimetría pulsada y la estimación magnética usando conjuntos atómicos magnéticos via el efecto de Faraday, esta técnica de filtraje de función patrón puede ser fácilmente usada para sondear conjuntos atómico-magéticos en ambientes con fuerte ruido técnico.

Contents

Chapter 1

Introduction

Balanced detection provides a unique tool for many physical, biological and chemical applications. In particular, it has proven useful for improving the coherent detection in telecommunication systems [1, 2], in the measurement of polarization squeezing [3, 4, 5, 6, 7], for the detection of polarization states of weak signals via homodyne detection [8, 9], and in the study of light-atom interactions [10]. Interestingly, balanced detection has proved to be useful when performing highly sensitive magnetometry [11, 12], even at the shot-noise level, in the continuous-wave (CW) [13, 14] and pulsed regimes [15, 16].

The detection of light pulses at the shot-noise level with low or negligible noise contributions, namely from detection electronics (electronic noise) and from intensity fluctuations (technical noise), is of paramount importance in many quantum optics experiments. While electronic noise can be overcome by making use of better electronic equipment, technical noise requires special techniques, such as balanced detection and spectral filtering.

Even though several schemes have been implemented to overcome these noise sources [17, 18, 19], an optimal shot-noise signal recovery technique that can deal with both technical and electronic noises, has not been presented yet. In this document, we provide a new tool based both on balanced detection and on the precise calculation of a specific pattern function that allows the optimal, shot-noise limited,

signal recovery by digital filtering. To demonstrate its efficiency, we implement a pattern-function filtering in the presence of strong technical and electronic noises. We demonstrate that up to 10 dB of technical noise for the highest average power of the beam, after balanced detection, can be removed from the signal. This is especially relevant in the measurement of polarization-rotation angles, where technical noise cannot be completely removed by means of balanced detectors [20]. Furthermore, we show that our scheme outperforms the Wiener filter, a widely used method in signal processing [21].

Optical readout of magnetic atomic ensembles have become the most sensitive instrument on Earth for measuring the magnetic field [11, 12]. Most prominent among the magneto-optical effects are the Faraday and the Voigt effects, which interactions of near-resonant light with the atomic vapor have demonstrated sensitivities better that $1\text{ft}/\sqrt{\text{Hz}}$ [22, 23]. The magnetic field is retrieved monitoring the polarization of the transmitted light beam [10], and when is used a balanced detector for measuring the polarization, the method has intrinsic advantages, in the sense that this configuration can be used to performed shot-noise limited measurements [13, 16], and also has the intrinsic ability to detect very small polarization-rotation angles. Also Faraday rotation, in the last years, have been used for spectral filtering using several schemes and techniques [24, 25, 26, 27] making relevant to measure with high accurancy those angles.

This thesis is organized as follows. In chapter 2 we present the theoretical model of our model-based technique for pattern-function filtering technical an electronic noise. In chapter 3 we show the operation of this tool by designing and implementing an experiment, where high amount of noise (technical and electronic) is filtered. In chapter 4 we show how can be used our tool for pulsed polarimetry, retrieving and optimal estimation on the polarization-rotation angle. Finally in chapter 5 we present the conclusions, summarizing the main results and the possible implications of this work.

1.1 Publications

The work presented in this thesis was acknowledged in the following publication [28]:

- Yannick A. de Icaza Astiz, Vito Giovanni Lucivero, R. de J. León-Montiel, Morgan W. Mitchell, *Optimal signal recovery for pulsed balanced detection*, Phys. Rev. A. **90**, 033814–(2014).

The author participated in many other experiments not shown in this thesis, this led to some publishable results [29, 30, 25, 31, 32]:

- Y. A. de Icaza Astiz, *Binary coherent beam combining with semiconductor tapered amplifiers at 795 nm,* Master's thesis, Msc in Photonics. Universidad Politécnica de Cataluña, Barcelona Tech. Available at http://upcommons.upc.edu/ (2009).
- F. A. Beduini, N. Behbood, Y. de Icaza, B. Dubost, M. Koschorreck, M. Napolitano, A. Predojević, R. Sewell, F. Wolfgramm, and M. W. Mitchell, *Quantum metrology with atoms and photons,* Opt. Pura Apl. **44**, (2) 315–323 (2011).
- F. Wolfgramm, Y. A. de Icaza Astiz, F. A. Beduini, A. Cerè and M. W. Mitchell, *Atom-resonant heralded single photons by interaction-free measurement,* Phys. Rev. Lett. **106**, 053,602 (2011).
- F. A. Beduini, J. A. Zielińska, V. G. Lucivero, Y. A. de Icaza Astiz, M. W. Mitchell, *Interferometric measurement of the biphoton wave function*, Phys. Rev. Lett. **113**, 183,602- (2014).
- F. A. Beduini, J. A. Zielińska, V. G. Lucivero, Y. A. de Icaza Astiz, M. W. Mitchell, *A macroscopic quantum state analysed particle by particle*, arXiv **quant-ph** 1410.7079v1 (2014).

Chapter 2

Theoretical model for optimal signal recovery

In this chapter, we introduce the theoretical framework of the filtering technique and show how optimal pulsed signal recovery can be achieved. In order to optimally recover a pulsed signal in a balanced detection scheme, it is necessary to characterize the detector response, as well as the "electronic" and "technical" noise contributions [33].

This chapter is organized as follows. In section 2.1 we present the model that we use for a balanced detector. In section 2.2, we introduce the form of the *signal recovery estimator*, together with the *pattern function*. In section 2.3, we obtain the conditions that should satisfy the pattern function. In section 2.3.1, we introduce the noise model that describes the technical noise in our system. In section 2.4, we obtain an analytical expression for the pattern function.

We leave for chapter 3 an experimental test on the pattern function together with all the experimental considerations.

2.1 Model for a balanced detector

To model a balanced detector, see Fig. 2.1, we assume that it consists of 1) a polarizing beam splitter (PBS), which splits the H and V polarization components heading toward 2) two detectors PD_H and PD_V, whose output currents are directly subtracted, and 3) a linear amplifier.

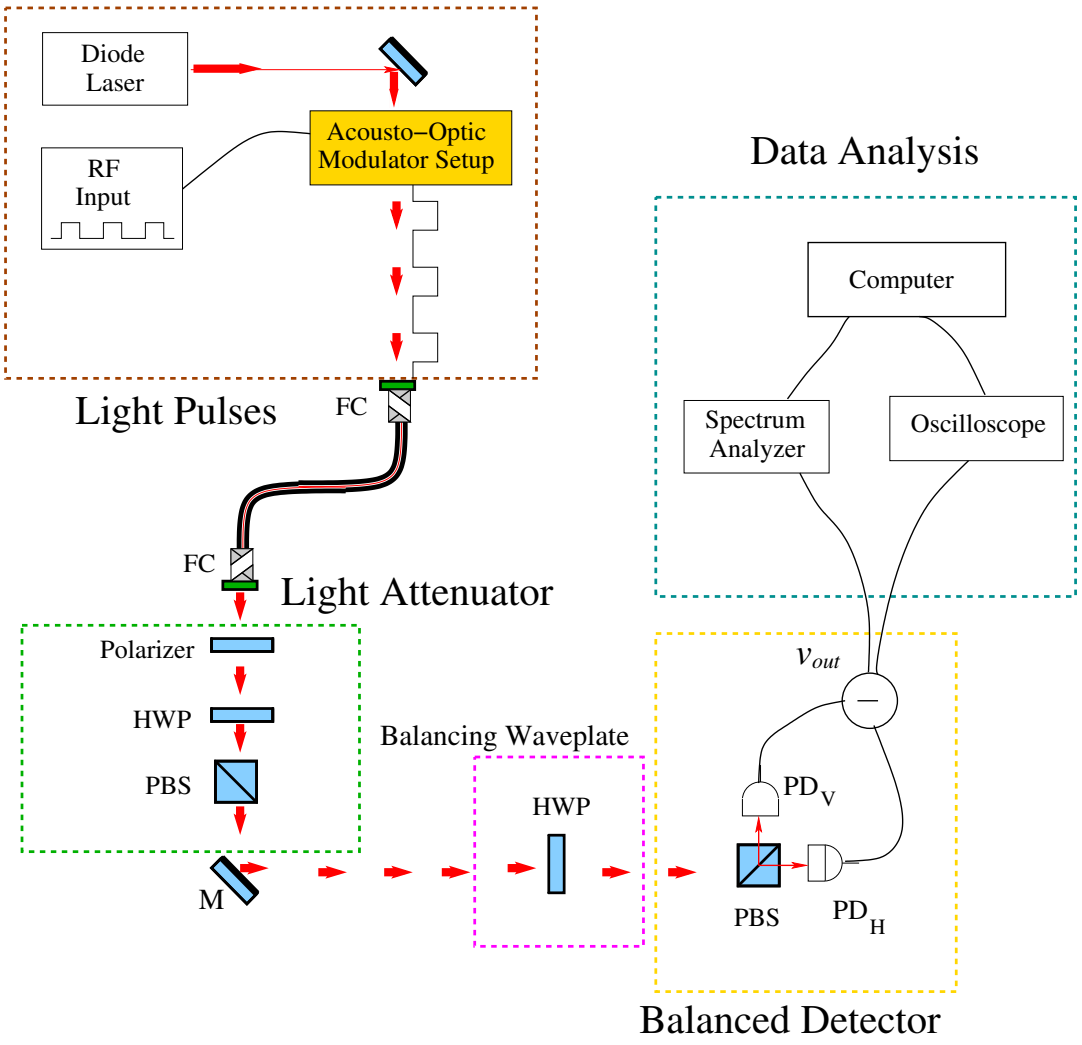

Figure 2.1: Experimental setup. M, mirror, FC, fiber coupling, HWP, half-wave plate. See section 3.4.3 for details on the experimental setup.

Because the amplification is linear and stationary, we can describe the response of the detector by impulse response functions $h(\tau)$. If the photon flux at detector X is $\phi_X(t)$, the electronic output can be defined as

$$v_{\text{out}}(t) \equiv h_H * \phi_H + h_V * \phi_V + v_N(t), \tag{2.1}$$

where v_N is the electronic noise of the photodiodes, including amplification. Here, $h * \phi$ stands for the convolution of h and ϕ, i.e., $(h * \phi)(t) \equiv \int_{-\infty}^{\infty} h(t-\tau)\phi(\tau)d\tau$. For clarity, the time dependence will be suppressed when possible. It is convenient to introduce the following notation: $\phi_S \equiv \phi_H + \phi_V$, $\phi_D \equiv \phi_H - \phi_V$, $h_S \equiv h_H + h_V$ and $h_D \equiv h_H - h_V$. Using these new variables, Eq. (2.1) takes the form

$$v_{\text{out}}(t) = \frac{1}{2}\left(h_S * \phi_S + h_D * \phi_D\right) + v_N(t). \tag{2.2}$$

From this signal, we are interested in recovering the differential photon number S with minimal uncertainty, where S is defined as

$$S \equiv \int_{\mathcal{T}} \phi_H(t)dt - \int_{\mathcal{T}} \phi_V(t)dt, \tag{2.3}$$

where $\mathcal{T}$ is the time interval of the desired pulse. More precisely, we look for an unbiased estimator $\hat{S}[v_{\text{out}}(t)]$, i.e. $\langle \hat{S} \rangle = \langle S \rangle$ with minimal variance var $(\hat{S})$.

2.2 Signal recovery estimator

To meet the unbiased condition on $\hat{S}$, it must be a linear function of v_{out}. This because S and v_{out} —Eqs. (2.3) and (2.1)— are linear in both ϕ_H and ϕ_V, meaning that it must be given by

$$\hat{S} = \int_{-\infty}^{\infty} v_{\text{out}}(t)\gamma(t)dt. \tag{2.4}$$

In Eq. (2.4), $\gamma(t)$ stands as *the pattern function* describing the most general linear estimator. In this work, we will consider three cases: 1) a raw estimator, $\gamma(t) = 1$; 2) a Wiener estimator, which makes use of a Wiener-filter-like pattern function, $\gamma(t) = w(t)$, where

$w(t)$ represents the Wiener filter in the time domain [21], and 3) a model-based pattern function estimator $\gamma(t) = g(t)$. Notice that both $w(t)$ and $g(t)$ are defined in $(-\infty, \infty)$, allowing to properly choose a desired pulse. In what follows, we explicitly show how to calculate the model-based pattern function estimator $g(t)$.

2.3 Conditions of the pattern function

We assume that ϕ_S, ϕ_D have known averages (over many pulses) $\bar{\phi}_S(t), \bar{\phi}_D(t)$, and similarly the response functions $h_S(\tau), h_D(\tau)$ have averages $\bar{h}_S(\tau), \bar{h}_D(\tau)$. Then the average of the electronic output reads as

$$\bar{v}_{out}(t) = \frac{\overline{h}_S * \overline{\phi}_S + \overline{h}_D * \overline{\phi}_D}{2}, \tag{2.5}$$

and $\langle \hat{S} \rangle = \int_{-\infty}^{\infty} dt\, g(t) \left(\bar{h}_S * \bar{\phi}_S + \bar{h}_D * \bar{\phi}_D \right)/2$. In writing Eq. (2.5), we have assumed that the noise sources are uncorrelated.

From this we observe that if a balanced optical signal is introduced, i.e. $\bar{\phi}_D = 0$, the mean electronic signal $\bar{v}_{out}(t)$ is entirely due to $\overline{h}_S * \overline{\phi}_S$. In order that $\hat{S}$ correctly detects this null signal, $g(t)$ must be orthogonal to $\overline{h}_S * \overline{\phi}_S$, i.e.

$$\int_{-\infty}^{\infty} g(t) \cdot \left(\overline{h}_S * \overline{\phi}_S \right)(t) dt = 0. \tag{2.6}$$

Our second condition may be seen to follow from

$$\int_{-\infty}^{\infty} g(t) \cdot \left(\overline{h}_D * \overline{\phi}_D \right)(t) dt = \int_{\mathcal{T}} \overline{\phi}_D(t) dt, \tag{2.7}$$

which is in fact a calibration condition: the right-hand side is a uniform-weight integral of $\overline{\phi}_D$, while the left-hand side is a non-uniform-weight integral, giving preference to some parts of the signal. If the total weights are the same, the above condition gives $\langle \hat{S} \rangle = \langle S \rangle$. We note that this condition is not very restrictive. For example, given $\bar{h}, \bar{\phi}$, and given $g(t)$ up to a normalization, the equation simply specifies the normalization of $g(t)$.

Notice that the condition given by Eq. (2.7) may still be somewhat ambiguous. If we want this to apply for all possible shapes $\bar{\phi}_D(t)$, it would imply $g(t) = \text{const.}$, and would make the whole exercise trivial. Instead, we make the physically reasonably assumption that the input pulse, with shape $\bar{\phi}_S$ is uniformly rotated to give $\bar{\phi}_H(t)$, $\bar{\phi}_V(t) \propto \bar{\phi}_S$. Similarly, it follows that $\bar{\phi}_D(t) \propto \bar{\phi}_S$. We note that this assumption is not strictly obeyed in our experiment and is a matter of mathematical convenience: a path difference from the PBS to the two detectors will introduce an arrival-time difference giving rise to opposite-polarity features at the start and end of the pulse, as seen in Fig. 3.5(a). A delay in the corresponding response functions h is, however, equivalent, and we opt to absorb all path delays into the response functions. In our experiment the path difference is ≈ 5 cm, implying a time difference of less than 0.2 ns, much below the smallest features in Fig. 3.5(a). Absorbing the constant of proportionality into $g(t)$, which comes from Eq. (2.7) and the relation $\bar{\phi}_D(t) \propto \bar{\phi}_S$, we find

$$\int_{-\infty}^{\infty} g(t) \cdot \left(\overline{h}_D * \overline{\phi}_S\right)(t)dt = \int_{\mathcal{T}} \overline{\phi}_S(t)dt, \tag{2.8}$$

which is our calibration condition.

2.3.1 Noise model

We consider two kinds of technical noise: fluctuating detector response and fluctuating input pulses. We write the response functions in the form $h_X = \bar{h}_X + \delta h_X$, for a given detector X, where the fluctuating term δh_X is a stochastic variable. Similarly, we write $\phi_Y = \bar{\phi}_Y + \delta\phi_Y$, where Y is H, V, S or D. By substituting the corresponding fluctuating response functions into Eq. (2.2), the electronic output signal becomes

$$
\begin{aligned}
v_{out}(t) &= \frac{1}{2}\left(\overline{h}_S * \overline{\phi}_S + \overline{h}_D * \overline{\phi}_D\right) + v_N(t) \\
&\quad + \frac{1}{2}\left(\delta h_S * \overline{\phi}_S + \delta h_D * \overline{\phi}_D\right) \\
&\quad + \frac{1}{2}\left(\overline{h}_S * \delta\phi_S + \overline{h}_D * \delta\phi_D\right) + O(\delta h\, \delta\phi) \qquad (2.9) \\
&\approx \frac{1}{2}\left(\overline{h}_S * \overline{\phi}_S + \overline{h}_D * \overline{\phi}_D\right) + v_N(t) + v_T(t), \qquad (2.10)
\end{aligned}
$$

where $v_T(t) \equiv \frac{1}{2}(\delta h_S * \overline{\phi}_S + \delta h_D * \overline{\phi}_D + \overline{h}_S * \delta\phi_S + \overline{h}_D * \delta\phi_D)$ is the summed technical noise from both δh and $\delta\phi$ sources. We note that the optical technical noise, in contrast to optical quantum noise, scales as $\mathrm{var}\,(\delta\phi) \propto \bar{\phi}^2$, so that $\mathrm{var}\,(v_T) \propto \bar{\phi}^2$. In passing to the last line we neglect terms $O(\delta h\, \delta\phi)$ on the assumption $\delta h \ll \bar{h}$, $\delta\phi \ll \bar{\phi}$. We further assume that v_N and v_T are uncorrelated.

We find the variance of the model-based estimator, $N_\sigma \equiv \mathrm{var}\,(\hat{S}_{\mathrm{opt}})$, is

$$
N_\sigma = \left\langle \left| \int_{-\infty}^{\infty} g(t) v_T(t) dt \right|^2 \right\rangle + \left\langle \left| \int_{-\infty}^{\infty} g(t) v_N(t) dt \right|^2 \right\rangle, \qquad (2.11)
$$

with the first term describing technical noise, and the second one electronic noise.

To compare against noise measurements, we transform Eq. (2.11) to the frequency domain. We note the inner-product form of Parseval's theorem

$$
\int_{-\infty}^{\infty} g^*(t) x(t) dt = \int_{-\infty}^{\infty} G^*(\omega) X(\omega) d\omega, \qquad (2.12)
$$

where the functions $G(\omega), X(\omega)$ are the Fourier transforms of $g(t), x(t)$, respectively. For any stationary random variable $x(t)$, $\langle X(\omega) X(\omega')\rangle = \delta(\omega - \omega')$ (if this were not the case, there would be a phase relation between different frequency components, which contradicts the assumption of stationarity). From this, it follows that

$$
\left\langle \left| \int_{-\infty}^{\infty} g(t) x(t) dt \right|^2 \right\rangle = \int_{-\infty}^{\infty} |G(\omega)|^2 \langle |X(\omega)|^2 \rangle d\omega. \qquad (2.13)
$$

Then, using Eq. (2.13), we can write the noise power as

$$N_\sigma = \int_{-\infty}^{\infty} |G(\omega)|^2 \langle |V_T(\omega)|^2 + |V_N(\omega)|^2 \rangle d\omega. \tag{2.14}$$

Our goal is now to find the $G(\omega)$ that minimizes N_σ satisfying the conditions in Eqs. (2.6) and (2.8), which in the frequency space are

$$I_{\text{or}} \equiv \int_{-\infty}^{\infty} d\omega\, G^*(\omega) \overline{H}_S(\omega) \overline{\Phi}_S(\omega) = 0, \tag{2.15}$$

$$I_{\text{cal}} \equiv \int_{-\infty}^{\infty} d\omega\, G^*(\omega) \overline{H}_D(\omega) \overline{\Phi}_S(\omega) = \overline{\Phi}_S(0). \tag{2.16}$$

Equations (2.15) and (2.16) describe, in the frequency domain, the orthogonality and the calibration conditions, respectively.

2.4 Solution

We will minimize the noise power N_σ (see Eq. (2.14)) with respect to the pattern function $G(\omega)$ using the two conditions (see Eq. (2.15) and Eq. (2.16)). We solve this by the method of Lagrange multipliers. For this, we write

$$L(G, \lambda_1, \lambda_2) = N_\sigma + \lambda_1 (I_{\text{or}} - 0) + \lambda_2 (I_{\text{cal}} - \overline{\Phi}_S(\omega = 0)), \tag{2.17}$$

and then solve the equations

$$\begin{aligned} \partial_{G^*} L &= 0, \\ \partial_{\lambda_1} L &= 0, \\ \partial_{\lambda_2} L &= 0. \end{aligned} \tag{2.18}$$

The first equation reads

$$\begin{aligned} \partial_{G^*} L &= G(\omega)\langle |V_T(\omega)|^2 + |V_N(\omega)|^2\rangle \\ &\quad +\lambda_1 \overline{H}_S(\omega)\overline{\Phi}_S(\omega) + \lambda_2 \overline{H}_D(\omega)\overline{\Phi}_D(\omega) = 0, \end{aligned} \tag{2.19}$$

with formal solution

$$G(\omega) = \frac{\lambda_1 \overline{H}_S(\omega)\overline{\Phi}_S(\omega) + \lambda_2 \overline{H}_D(\omega)\overline{\Phi}_D(\omega)}{\langle |V_T(\omega)|^2\rangle + \langle |V_N(\omega)|^2\rangle}. \tag{2.20}$$

The second and third equations from Eq. (2.18) are the same as Eq. (2.15) and Eq. (2.16) above. The problem is then reduced to finding λ_1, λ_2 which (through the above), make $G(\omega)$ satisfy the two constraints.

Substituting Eq. (2.20) into Eq. (2.15) and Eq. (2.16), we find

$$O_1\lambda_1 + O_2\lambda_2 = 0, \tag{2.21}$$

and

$$C_1\lambda_1 + C_2\lambda_2 = \Phi_0. \tag{2.22}$$

where

$$O_1 \equiv \int_{-\infty}^{\infty} \frac{|\overline{H}_S(\omega)|^2 |\overline{\Phi}_S(\omega)|^2}{\langle |V_T(\omega)|^2\rangle + \langle |V_N(\omega)|^2\rangle} d\omega, \tag{2.23}$$

$$O_2 \equiv \int_{-\infty}^{\infty} \frac{\overline{H}_D^*(\omega)\overline{\Phi}_S^*(\omega) \cdot \overline{H}_S(\omega)\overline{\Phi}_S(\omega)}{\langle |V_T(\omega)|^2\rangle + \langle |V_N(\omega)|^2\rangle} d\omega, \tag{2.24}$$

$$C_1 \equiv \int_{-\infty}^{\infty} \frac{\overline{H}_S^*(\omega)\overline{\Phi}_S^*(\omega) \cdot \overline{H}_D(\omega)\overline{\Phi}_S(\omega)}{\langle |V_T(\omega)|^2\rangle + \langle |V_N(\omega)|^2\rangle} d\omega, \tag{2.25}$$

$$C_2 \equiv \int_{-\infty}^{\infty} \frac{|\overline{H}_D(\omega)|^2 |\overline{\Phi}_S(\omega)|^2}{\langle |V_T(\omega)|^2\rangle + \langle |V_N(\omega)|^2\rangle} d\omega, \tag{2.26}$$

with $\Phi_0 \equiv \overline{\Phi}_S(\omega = 0)$. The solution to the set of Eqs. (2.21) and (2.22) is then given by

$$\lambda_1 = \frac{\Phi_0 O_2}{C_1 O_2 - C_2 O_1}, \quad \lambda_2 = \frac{\Phi_0 O_1}{C_2 O_1 - C_1 O_2}. \tag{2.27}$$

It should be noted that quantum noise is not explicitly considered in the model. Rather, it is implicitly present in ϕ_H, ϕ_V which may differ from their average values $\bar{\phi}_H, \bar{\phi}_V$ due to quantum noise. Note that the point of this measurement design is to optimize the measurement of $\int_{\mathcal{T}} \phi_H(t) - \phi_V(t)dt$, including the quantum noise in that variable. For this reason, it is sufficient to describe, and minimize, the other contributions.

Chapter 3

Experiment on optimal signal recovery

In this chapter we review the techniques and methods used for doing the experiment on "*optimal signal recovery for pulsed balanced detection*". The aim of this experiment is to test and demonstrate the theory shown in chapter 2.

This chapter is organized as follows. In section 3.1, we show how to produce the pulses of light, presenting their shapes and properties. In section 3.2, we present the detector that we use to measure the pulses and how it is characterized. In section 3.3, we introduce the theory for computing a power spectral density using a time-domain instrument like an oscilloscope. In section 3.4, we show experimentally that our detector is shot-noise limited using CW light. In section 3.5, we illustrate how to introduce technical noise in a controlled manner in our system. In section 3.6, we calculate the optimal pattern function for different optical power. In section 3.7, we show shot-noise limited detection using pulses and also the measurement of technically-noise limited pulses. In section 3.8, we demonstrate that using the pattern function we filter the 10 dB of technical noise, after balanced detection.

We leave for chapter 4 a comparison with the Wiener filter, a widely used method in signal processing [21]. Also this experimental

system can be used for measuring Faraday rotation on ensembles of Rubidium atoms, or to determining polarization-rotation angles, such results are on chapter 4.

Although some of the steps to perform the experiment are well known in the area of quantum optics, we decide to present a short definition or introduction in each of them.

3.1 Production of pulses of light

In our experimental setup, pulsed signals are produced using an external cavity diode laser at 795 nm (Toptica DL100), modulated by two acousto-optic modulators (AOMs) in series. We have used two AOMs to prevent a shift in the optical frequency of the pulses, and also to ensure a high extinction ratio ($r_e > 10^7$). In what remains of the section we detail how we produce the optical pulses, from a short introduction to the AOMs to the different shapes and properties.

Acousto-Optic Modulators

An acousto-optic modulator (AOM) consists of an optical medium, a piezoelectric transducer (PZT) and a sound absorber [34, 35]. Such devices are used for several applications: shifting of the main frequency by a radio-frequency (RF), deflection of the beam, producing light pulses, and attenuation of beams. A RF signal is sent into the PZT attached to the crystal, creating sound waves with frequencies of the order of 100 MHz, the sound absorber is used to eliminate the residual mechanical wave.

The physical principle in which is based the functioning of an AOM is *Bragg diffraction*. Light is diffracted at the traveling periodic refractive index grating generated by the sound wave, as can be seen in Fig. 3.1. Where we have represented the crests of the traveling sound waves that increase the refractive index (with a sound velocity v and a wavelength Λ). For an optical wavelength λ and θ the angle of the incident (scattered) ray with the acoustic wave-

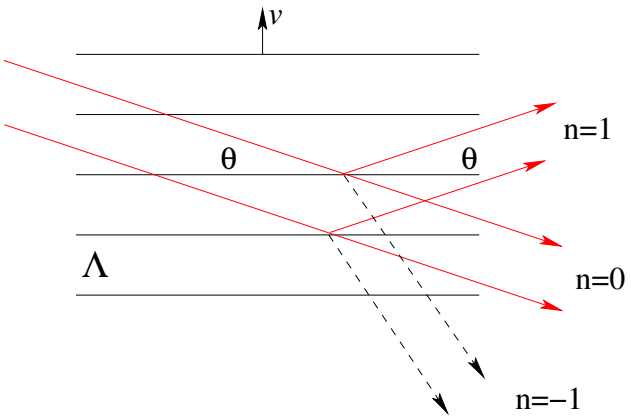

Figure 3.1: Bragg construction

front, the constructive interference on the scattered light is satisfied, in what is called the Bragg's law:

$$n\lambda = 2\Lambda \sin\theta. \tag{3.1}$$

The deflected photons experience a change of frequency, this change of frequency is proportional to the deflection angle. The deflection angle Θ is equal to 2θ, from the Bragg's condition. A change in the deflection angle $\Delta\Theta$ is connected with a change in the frequency Δf of the scattered light in the following way:

$$\Delta\Theta = \frac{\lambda}{v}\Delta f, \tag{3.2}$$

where v is the velocity of sound in the material.

The deflected beam is produced each time that there is an acoustic wave present in the material, so we can produce pulses of light using this fact, modulating or chopping the RF input signal, of course with the sound speed of the material as ultimate limit. We use two "Gooch & Housego" 46080-1-LTD acousto-optic deflectors. The interaction material is TeO_2, the sound speed for the shear wave is 617 m/s, limiting the rise time of the pulse to 150 ns/mm beam diameter [36, 37]. This device is polarization-independent due that the acoustic movement is in the direction of the light (shear wave), however the diffracted light compared to the input power is less efficient,

also depending on the beam shape, it is more efficient with a larger beam diameter that with a shorter one. Still the measured diffraction efficiency of each AOM is about 70%.

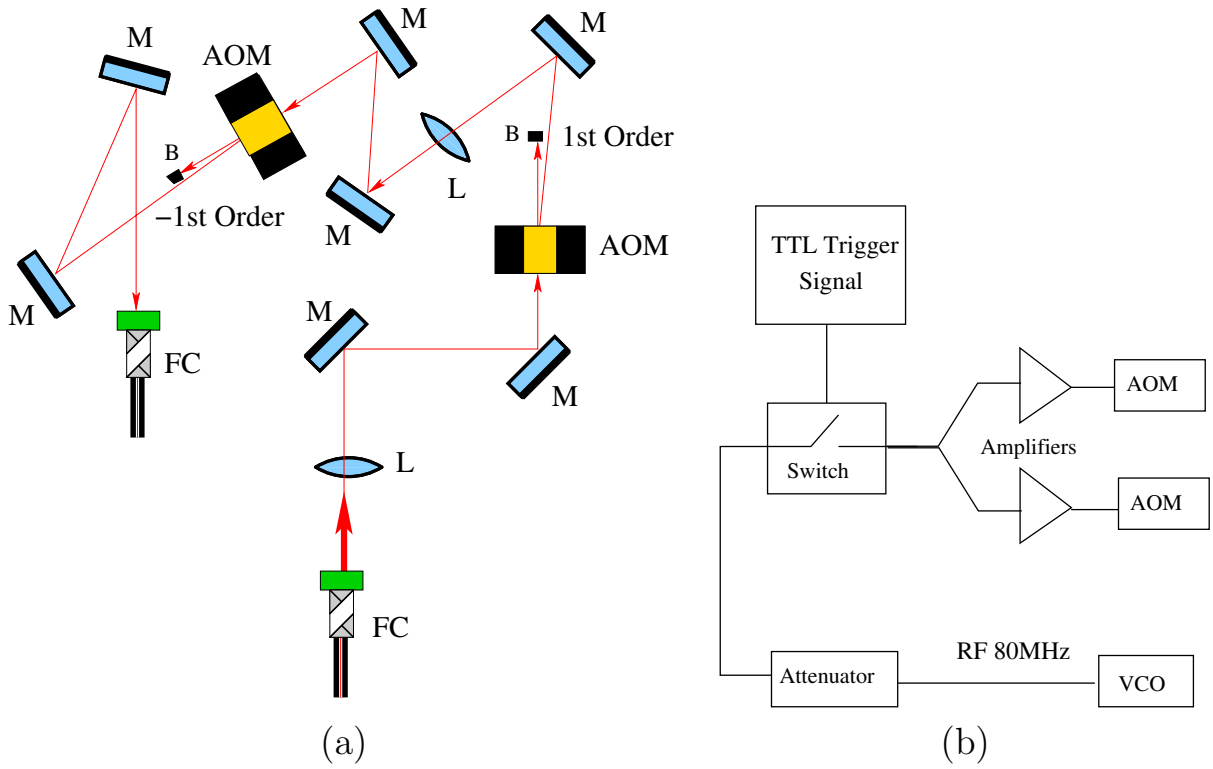

Figure 3.2: (a) Setup for producing pulses of light without a frequency shift using two Acousto-Optic Modulators. M: Mirror, L: Lens, B: Beam Blocker, FC: Fiber Coupling, AOM: Acousto-Optic Modulator. See Fig. C.1 for a picture of the lab setup. (b) Basic circuit for feeding the AOMs. VCO: Voltage Controlled Oscillator, TTL: Transistor-Transistor Logic.

Producing Pulses of Light without a frequency shift using two Acousto-Optic Modulators (AOM System)

It is possible to produce pulses of light at the deflection angle Θ, but because of Eq. (3.2), these pulses experience a change in frequency. For producing pulses of light of the same frequency of the input beam we use two AOMs, we align the first one optimizing the first order of the diffraction of the Bragg modes, and we align the second one optimizing the minus first order of the diffraction, see Fig. 3.2(a). In this way, the output pulses have the same frequency as the input ones.

The advantage of producing pulses of the same input frequency is that we could use these pulses in an homodyne measurement, because for an homodyne measurement both the local oscillator and the probe beam should have the same frequency.

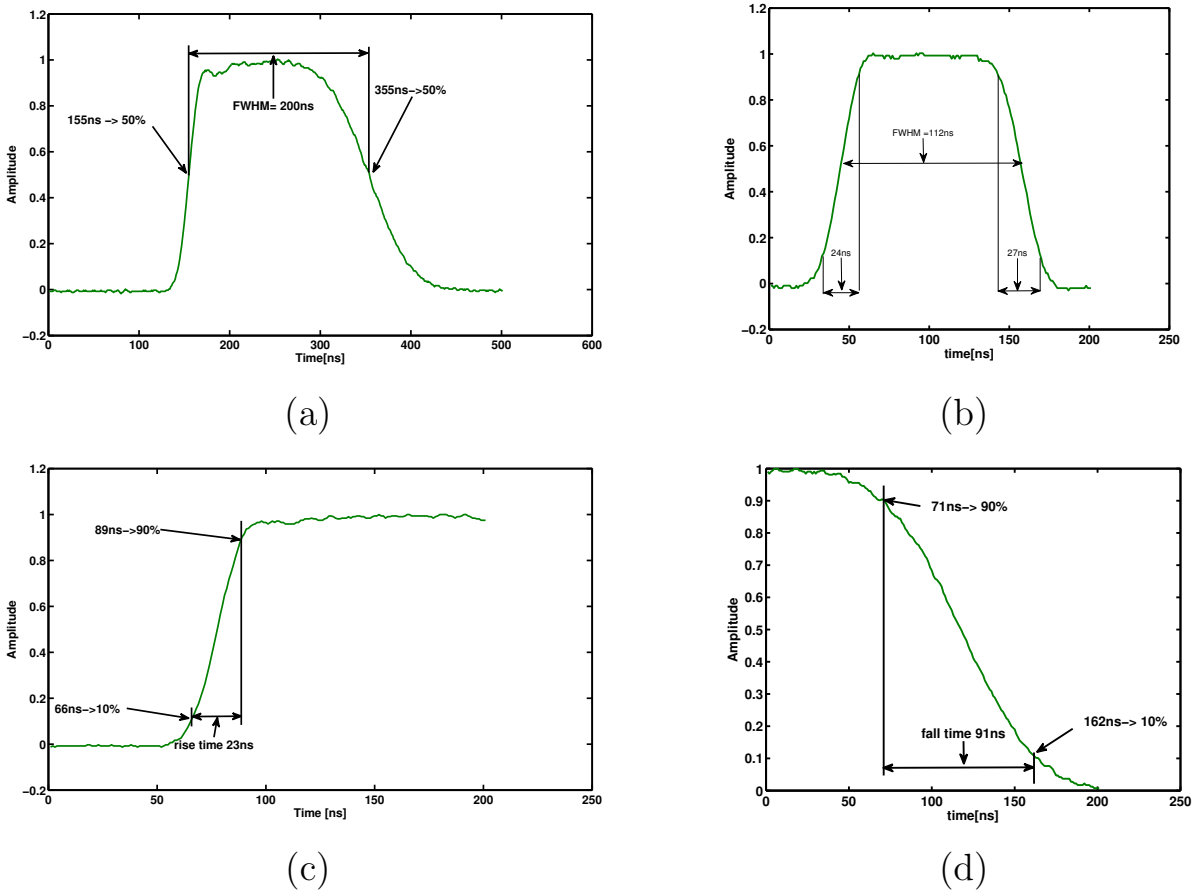

Figure 3.3: Different shapes of pulses and close up from the rise and fall times. (a) Asymmetrical pulse with fast rise time and slow fall time, (b) Symmetrical pulse, with both fast rise and fall times (steep pulse), (c) Close up of the fast rise time, (d) Close up for the slow fall time (relaxed pulse: a pulse with both slow rise and fall times).

We exploit and characterize two potential advantages of this AOM system that uses two AOMs. The first one is that we can create three different shapes of the output pulses, and the second one is that we have a high extinction ratio between the pulse on and the pulse off. We measure the whole efficiency of this setup from input fiber to output fiber, of course it depends on the alignment. The maximum efficiency that we can obtain is about 35%.

Different shapes of the output pulses. We design a setup for producing three different shapes of pulses, with different rise and fall times: both fast rise and fall times, both slow rise and fall times, fast rise time and slow fall time. The setup was calculated using the "*ray transfer matrix analysis*" [38]. The optical setup is composed of lenses L, mirrors M, beam blockers B and the two AOMs. It is shown in Fig. 3.3(a) and (b) two different shapes of pulses and in Fig. 3.3(c) and (d) the fast rise time and the slow fall time, respectively.

High extinction ratio of the pulse on versus the pulse off. For measuring the extinction ratio of the pulse on versus the pulse off, we use a lock-in amplifier (Stanford Research Systems model SR830 DSP), we obtained the following extinction ratios:

Asymmetrical Pulse. The light is deflected (in the first one into the 1st order and in the second one into the -1st order) and pulsed in both AOMs. Extinction ratio better than 1×10^{-7}, this measurement was limited by the instrument sensitivity, the signal for the pulse was smaller that the minimum sensitivity: 1×10^{-7}.

Steep Pulse. The first AOM is used to deflect (into the 1st order) and to pulse the light, but the second one is only used for deflecting the light (into the -1st order) without pulsing. Extinction ratio $6.4 \pm 0.2 \times 10^{-6}$.

Relaxed Pulse. The first AOM is used to deflect (into the 1st order) without pulsing, and the second AOM is used for deflecting (into the -1st order) and pulsing the light. Extinction ratio $1.24 \pm 0.3 \times 10^{-5}$.

3.2 Pulse detection and detector characterization

Balanced detection is performed by using a Thorlabs PDB150A detector [39] that contains two matched photodiodes wired back-to-

back for direct current subtraction, amplified by a switchable-gain transimpedance amplifier. We use the gain settings 10^3 V/A and 10^5 V/A, with nominal bandwidths of 150 MHz and 5 MHz, respectively. Figure 3.4(a) shows the average pulse shapes $p(t)$ and $p'(t)$, observed with bandwidth settings 150 MHz and 5 MHz, respectively. These shapes are obtained by blocking one detector and averaging over 1000 pulse traces (280 ns width).

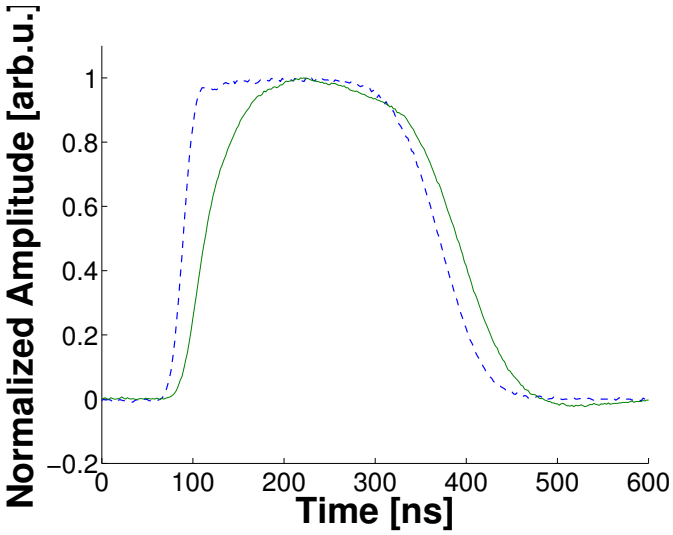

Figure 3.4: Average pulse shapes of the original pulse $p(t)$ at 150 MHz (blue dashed line) and the amplified one $p'(t)$ at 5 MHz (green solid line). For the sake of comparison, both pulses are normalized.

In this way, to determine the impulse response functions $h_H(t)$, $h_V(t)$ of the photodiodes PD_H and PD_V, respectively, we first assume the form

$$h_X(t) = \frac{e^{-t/\tau_{\mathrm{TIA}}} - e^{-t/\tau_X}}{\tau_{\mathrm{TIA}} - \tau_X}, \tag{3.3}$$

where $X \in \{H, V\}$ indicates the photodiode. This describes a single-pole filter with time constant τ_X for the photodiode [40, 41] followed by a single-pole filter with time-constant τ_{TIA} for the transimpedance amplifier. We choose the parameters $\tau_{\mathrm{TIA}}, \tau_X$ by a least-squares fit of

$$\tilde{p}'(t) \equiv \int_{-\infty}^{\infty} p(\tau) h_X(t-\tau) d\tau. \tag{3.4}$$

to the measured traces $p'(t)$ [42].

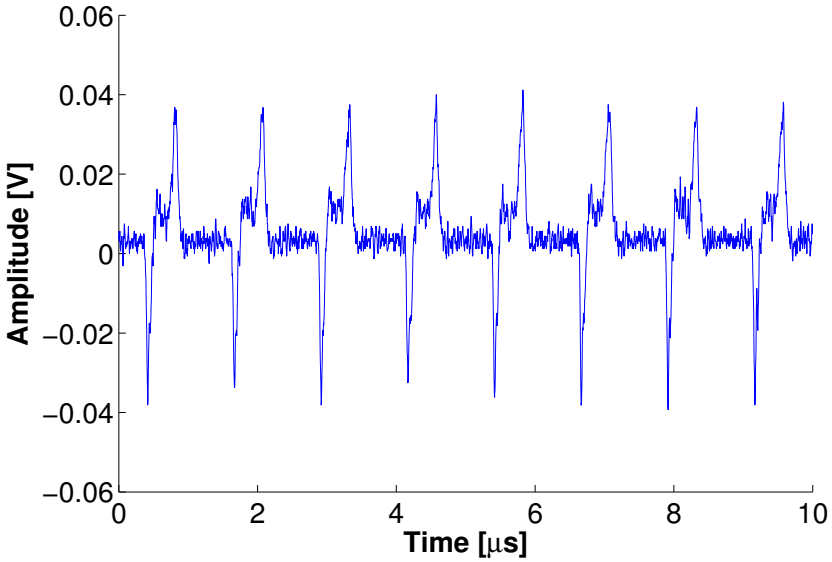

(a)

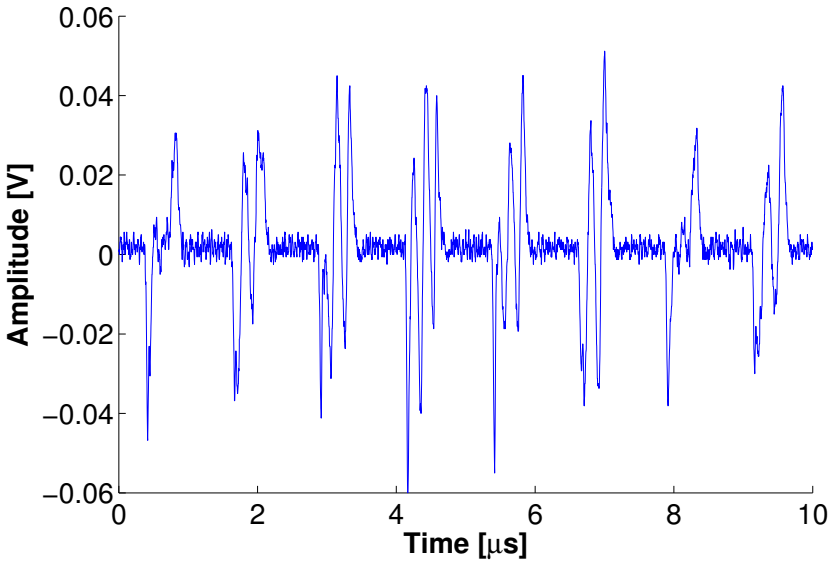

(b)

Figure 3.5: Example of pulses seen by the balanced detector (a) without technical noise, and (b) with technical noise introduced.

As seen in Fig. 3.5(a), a small difference in the speeds of the two detectors leads to electronic pulses with a negative leading edge and a positive trailing edge, even when the optical signal is balanced, i.e. even when the average electronic output is zero.

3.3 Power spectral density using the scope

The scope is a time-domain instrument, it is very useful to visualize time signals and to acquire data in the time domain. The standard approach for data analysis in the frequency domain is to use a Spectrum Analyzer or a new generation scope that incorporates utilities for computing the spectral density estimation. Nevertheless for the new tool that we want to develop, since it is a filter in the time domain, we use the scope and Matlab together for extracting the power spectral density (PSD). In the end we use the same instrument for the noise characterization and the optimization.

Matlab is very useful for processing lab data, and at least for the whole experiment was proved that was more suitable than Labview and Mathematica. Matlab has already functions that computes the Power Spectral Density (PSD) or mean-square spectrum estimate. We use the next two ones: periodogram and pwelch, these two functions are very robust and fast (in fact *periodogram* is faster, but has larger variances on the estimate). They need as inputs the string of the signal for which you want to obtain the PSD estimate, the sampling frequency of the data, a window function that is used to improve the fast Fourier transform process, and the overlap for *pwelch* function. Now, we sketch the main ideas of the calculation of the PSD and how to interpret the results of a PSD. The ideas presented in the next sections, and used for the calculations, were taken from [43, 21, 44, 45].

First, we define the basic concepts: Fourier transform, fast Fourier transform and the time and frequency resolutions. These concepts are inside the definitions of the functions that compute the PSD estimate. Secondly, we define the periodogram and the average periodograms, known as *Bartlett Method* and *Welch Method*, that leads to the pwelch function from Matlab.

3.3.1 Fourier transform and other definitions

The following definitions are only needed by consistency, we did all the calculations using Matlab, and using their definitions.

The Fourier transform, denoted by $F(\omega)$, of the function $f(t)$ is defined by

Definition 3.3.1 (Fourier Transform)

$$F(w) = \int_{-\infty}^{\infty} f(t)e^{-\mathbf{i}wx}dx \tag{3.5}$$

The inverse Fourier transform is defined by

Definition 3.3.2 (Inverse Fourier Transform)

$$f(t) = \frac{1}{2\pi}\int_{-\infty}^{\infty} F(w)e^{\mathbf{i}wx}dx. \tag{3.6}$$

Definition 3.3.3 (Fast Fourier Transform (Matlab))
The functions X=fft(x) and x=ifft(X) implement the transform and inverse transform pair given for vectors of length N by:

$$X(k) = \sum_{m=1}^{N} x(m)w_N^{(m-1)(k-1)}, \tag{3.7}$$

$$x(m) = \frac{1}{N}\sum_{k=1}^{N} X(k)w_N^{-(m-1)(k-1)}, \tag{3.8}$$

where $w_N = e^{\frac{-2\pi\mathbf{i}}{N}}$ is an N^{th} root of the unity.

Definition 3.3.4 (Frequency and Time Resolutions)
The scope has a intrinsic *maximum sampling frequency* and a *specific sampling frequency* F_S depending on the scale and the number of points that one can take. The *Nyquist frequency* is the half of the F_S. Referring to specific sampling frequency F_S and to the N number of points that one takes, one obtains the **frequency resolution** by

$$\Delta f = \frac{F_S}{N}. \tag{3.9}$$

The **time resolution**, in a period T, or in window of time T, is given by

$$\Delta t = \frac{T}{N} \tag{3.10}$$

These quantities are coupled in the next way

$$\Delta t = \frac{1}{F_S}, \quad \Delta f = \frac{1}{T}. \tag{3.11}$$

3.3.2 Periodogram and averaged periodograms

For a given signal $f(t)$, we can define the instantaneous power of the signal as $f^2(t)$, then the total energy of the signal is the integral of $f^2(t)$ over all time:

$$\mathsf{POW}\left[f(t)\right] = \int_{-\infty}^{\infty} f(t)^2 dt. \tag{3.12}$$

Using the Parseval's relation we obtain:

$$\mathsf{POW}\left[f(t)\right] = \int_{-\infty}^{\infty} |F(\omega)|^2 d\omega. \tag{3.13}$$

Now, let us define a filtered function $H(\omega)$ of the function $F(\omega)$ in the following way

$$H(\omega) = \left\{ \begin{array}{cc} F(\omega) & w \in [w_1, w_2] \\ 0 & \text{otherwise} \end{array} \right\}. \tag{3.14}$$

We can calculate the total energy in the filtered function $H(\omega)$

$$\mathsf{POW}\left[h(t)\right] = \int_{-\infty}^{\infty} |H(\omega)|^2 dt = \int_{\omega_1}^{\omega_2} |F(\omega)|^2 d\omega. \tag{3.15}$$

This is why, it makes sense to call $|F(\omega)|^2$ the *spectral power density of the signal* $f(t)$ [46]. We denote the task of obtaining the power spectral density from a signal $f(t)$ as $\mathsf{PSD}[f(t)]$. The function periodogram in Matlab computes this *spectral power density* from a discrete signal [44, 21].

We can average K periodograms $\mathsf{PSD}[f(t)]$ taken from K similar signals $f(t)$ and then obtaining an average. The resulting trace is known as *Bartlett periodogram*, having a strong reduction in the fluctuations of the trace.

Another averaged periodogram is obtained by the *Welch's method*, averaging periodograms from overlapped and windowed segments. The signal is divided into overlapping segments. The overlapping segments are windowed, enhancing the influence of the data at the central parts and reducing the influence of the data at the edges. For more details check the sources [45, 21].

We use Welch's method for characterizing our detection system, as can be seen in Fig. 3.6.

3.4 Shot-noise-limited detection for CW light

A balanced-amplified detector (Thorlabs PDB150A) with switchable-gain was used to detect squeezing in our lab in the past. A previous step to measure squeezing using a detector is to check that the detector is shot-noise limited. Step that was done by another PhD student [6, 47].

In the present section, first we verify that our detector is theoretically shot-noise limited using the parameters of the manufacturer, next we show experimentally that the detector is shot-noise limited. We test again that the detector is shot-noise limited and also we test the method of calculating the PSD presented in section 3.3, for checking consistency.

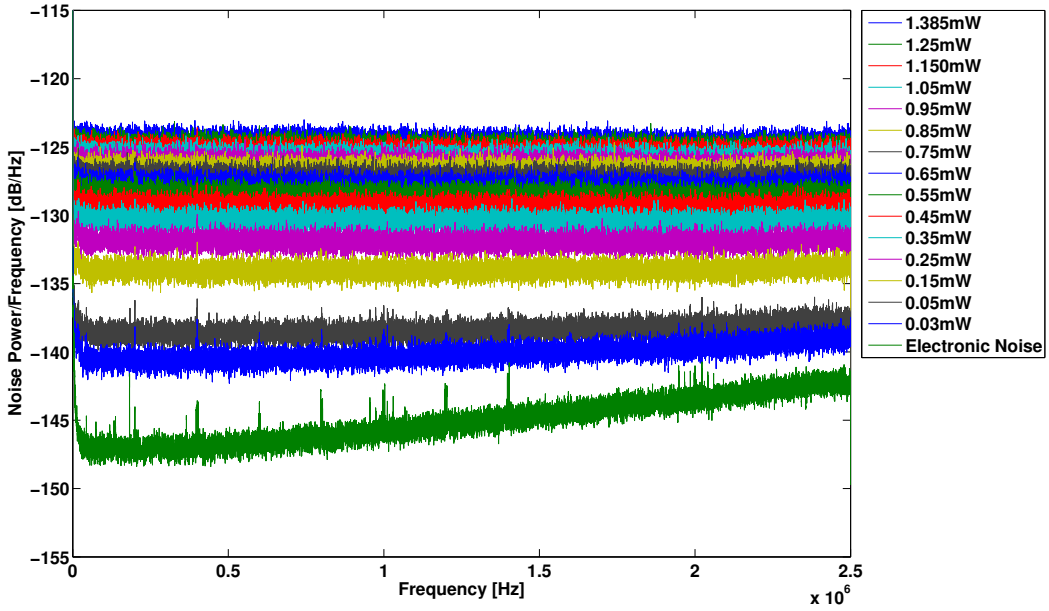

Figure 3.6: Power spectral density using the Welch's method for different input light powers. Here, it is shown frequencies from 0 to 2.5 MHz.

In Fig. 3.6 is shown the PSD for each power and each frequency from our detector showing that our detector is shot-noise limited. Now we proceed to detail the theory, definitions and the experimental test.

3.4.1 Theoretical description: Shot-noise-limited detection

The fundamental source of noise [33], the *shot noise* ΔI_{shot} [A], in the current arises because of the corpuscular character of the photons. The shot noise of an average current I is given by

$$\Delta I_{shot} = \sqrt{2eIB} \tag{3.16}$$

Where e is the electron charge and B is the bandwidth. Normally the bandwidth of the detector, or the bandwidth of the lowest filter involved in the measurement.

The optical shot noise ΔP_{shot} [W] is

$$\Delta P_{shot} = \sqrt{2h\nu \overline{P} B}. \tag{3.17}$$

Where h is the Plank constant, ν the frequency of the beam and $\overline{P}$ is the average optical power of the beam, and B is the bandwidth.

The second source of noise is the *thermal* or *Johnson noise* $\Delta I_{thermal}$.

$$\Delta I_{thermal} = \sqrt{\frac{4k_B T B}{R_{sh}}} \tag{3.18}$$

Where k_B is the Boltzmann constant, T is the temperature and R_{sh} is the shunt resistance.

There is another shot-noise contribution, *dark noise*, for the noise that produces the dark current I_{dark}, current produced in the absence of light in the detector.

$$\Delta I_{dark} = \sqrt{2eI_{dark}B} \tag{3.19}$$

The last contribution is the *amplifier noise* $\Delta I_{amplifier}$.

$$\Delta I_{amplifier} = \sqrt{2eGBF} \tag{3.20}$$

G is the voltage gain and F is the excess noise factor, a composite of different contributions inside the amplifier. The excess noise factor is normally quoted in the technical specifications.

The total noise is

$$\Delta I_{tot} = \sqrt{\Delta I_{shot}^2 + \Delta I_{dark}^2 + \Delta I_{thermal}^2 + \Delta I_{amplifier}^2}. \tag{3.21}$$

Definition 3.4.1 (Shot-noise-limited detection)
A detector for which $\Delta I_{electronic}^2 = \Delta I_{dark}^2 + \Delta I_{thermal}^2 + \Delta I_{amplifier}^2 \leq \Delta I_{shot}^2$ is named as "shot-noise-limited" detector. Because the noise is going to be limited by the shot noise of the input light, and not by the electronic noise.

A detector that is electronic-noise limited cannot be used for a quantum optics experiment, because you cannot detect the shot-noise of the light.

3.4.2 Experimental description: shot-noise-limited detection

In order to check that our detector is shot-noise limited we need to see the noise equivalent power (NEP) reported by the manufacturer and to see what is the threshold of optical power for producing the same amount of noise. Now we proceed to do this calculation.

The one-sided power spectral density of the optical power in the case of shot noise is $PSD_{optical} = 2h\nu\overline{P}$ [W^2/Hz] [35]. The shot noise per square root of bandwidth is $\Delta P_{shot/\sqrt{B}} = \sqrt{PSD_{optical}}$ [W/$\sqrt{\text{Hz}}$].

The noise equivalent power reported by the manufacturer in the manual is 0.6 pW/$\sqrt{\text{Hz}}$ [39]. Therefore from the table 3.1 our detector is shot noise limited for powers higher that 0.8 μW.

$\overline{P}$ [mW]	$\Delta P_{shot/\sqrt{B}}$ [pW/$\sqrt{\text{Hz}}$]
0.4	14.14
0.1	7.069
0.001	0.707
0.0008	0.6323

Table 3.1: Shot noise per $\sqrt{B}$ ($\Delta P_{shot/\sqrt{B}}$) vs optical power ($\overline{P}$)

Predojević [6, 47] measured the noise of our detector finding that the electronic noise of the whole system with 400 μW of input power was 14 dB below the shot-noise limit. This result is consistent with these calculations.

3.4.3 Experimental setup

From the Fig. 2.1, we use a DL-100 Toptica Laser [48], the central frequency is set to $\lambda = 794.9\ nm$ (D_1 transition of Rubidium 87) [49]. It is relevant to be at this wavelength for the potential applications of light interacting with ^{87}Rb [13, 47, 7, 50]. We couple the light into a single-mode fiber (for spacial cleaning of the mode), and we send this light to the AOM setup, described in section 3.1. Here, we produce

the light pulses using a basic RF circuit. The setup and the circuit are shown at Figs. 3.2(a) and 3.2(b), respectively. The output light of the AOM setup is coupled into a single-mode fiber, and sent to a polarizer, a Half-Wave Plate (HWP) and a Polarizing Beam Splitter (PBS). These three last elements are used for controlling the power of the beam. Next, we have a balancing HWP and finally the balanced detector is composed by a PBS, and the two photodiodes (PD_H and PD_V), which are inside the Thorlabs detector PDB150A.

As a summary, this setup can produce pulses of light without a frequency shift of the input light, these pulses are resonant with D1 line of ^{87}Rb, producing pulses with repetition rates from few mHz to 4 MHz, and three different shapes of pulses as shown in section 3.1. We can control the input power (Polarizer+ HWP+PBS) that is sent to the balanced detector (PBS + Balanced Detector). We can analyze the voltage produced at the balanced detector with a Spectrum Analyzer or with an Oscilloscope.

3.4.4 Shot-noise-limited detection

From Eq. (3.17), we can see that the variance of the optical power (the shot-noise squared) is proportional to the optical power:

$$\Delta P_{shot}^2 \propto \overline{P}. \tag{3.22}$$

From Eqs. (3.18), (3.19), (3.20) we can deduce that the electronic noise power does not depends on the optical power, we can write it like:

$$\Delta P_{elec}^2 \propto \overline{P}^0. \tag{3.23}$$

Then, making use of the setup presented in Fig. 2.1, and together with the technique presented in section 3.3 for obtaining the PSD using the scope. We obtain that our detector is shot-noise limited with a very good margin for high frequencies. The results of this measurement are presented in Fig. 3.6. Such results are consistent with previous observations done by Predojević [6, 47]. The observations done before were limited by the Spectrum Analyzer whose

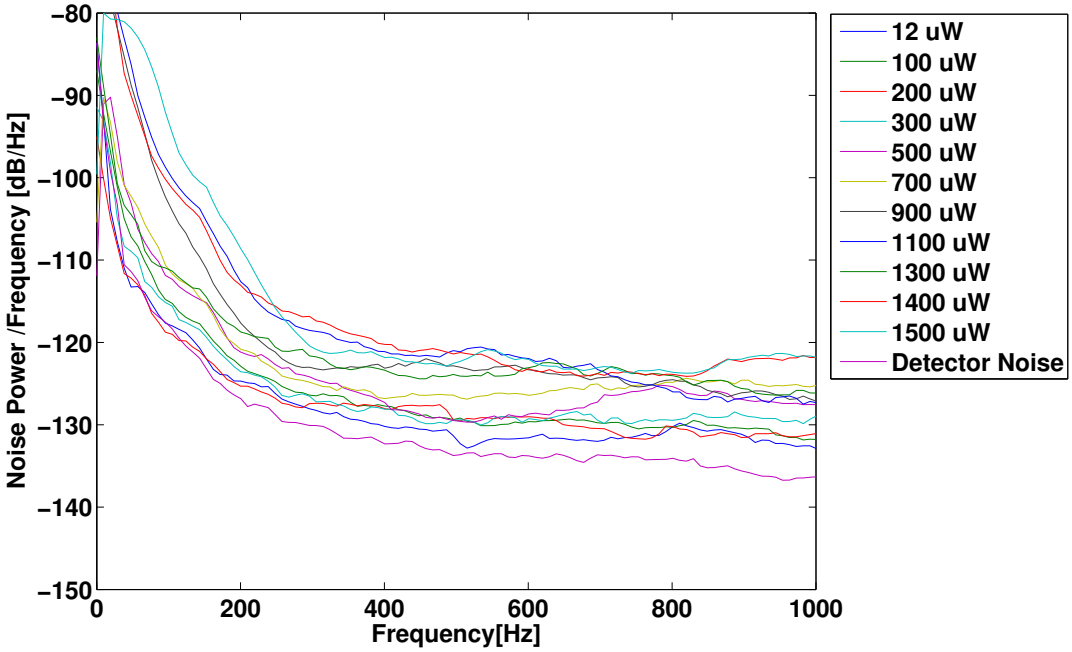

Figure 3.7: Power spectral density estimate using the Welch method for different input light powers. Here, it is shown frequencies from 0 to 1 kHz, it can be seen that below 300 Hz, it is not shot-noise limited.

minimum frequency was 9kHz [51]. Nevertheless, for us it is possible to go lower calculating the PSD using the data acquired using the scope, see section 3.3. Having data that is barely shot-noise limited for higher frequencies than 300 Hz, see Fig. 3.7.

Equations (3.22) and (3.23) can be combined into one equation

$$\Delta P^2_{total} = A + B \cdot \overline{P}. \tag{3.24}$$

Nevertheless, this last equation is not complete. There is another noise called *technical noise*, which are form by intensity-noise fluctuations, which are proportional to the optical power square [33]. Therefore the total noise power is

$$\Delta P^2_{total} = A + B \cdot \overline{P} + C\overline{P}^2. \tag{3.25}$$

In the next section we show how we produce technical noise in controlled way.

3.5 Producing technical noise in a controlled manner

In order to prove that it is possible to remove technical noise, first we need to produce it in a controlled manner. To this end, we introduce technical noise in our system perturbing the main frequency of the AOMs using the circuit described in Fig. 3.8. The main frequency is produced by a voltage controlled oscillator (VCO) set to 80 MHz. Then, it is split with a power splitter, one of the arms is mixed with a signal from an arbitrary wave generator (AWG) and attenuated, whereas in the other arm the signal is passed by a phase shifter. Finally, both signals are put back together with a power combiner. In this way, we have a main frequency of 80 MHz and sidebands at the frequency of the signal introduced with the AWG. We can then program the AWG with technical noise for a particular frequency and bandwidth, as illustrated in Fig. 3.9, for introducing an arbitrary functions into the AWG we follow the protocol from the appendix B.

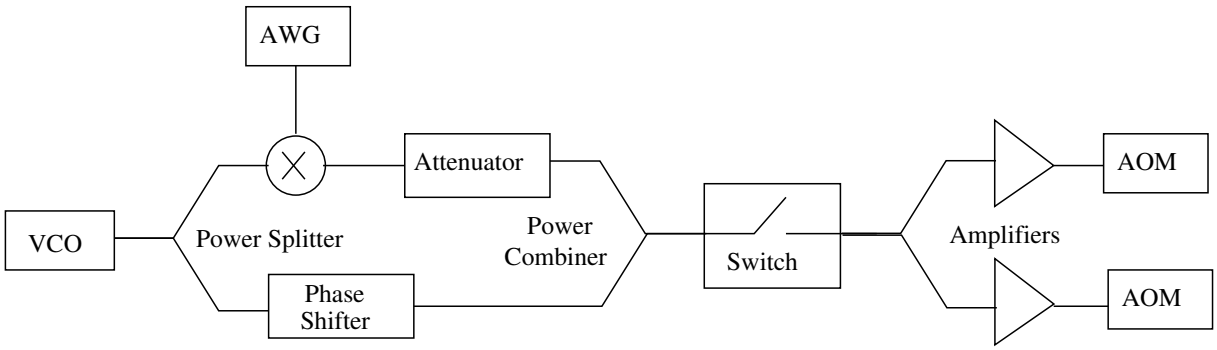

Figure 3.8: Scheme of the electronic circuit used to introduce technical noise into the AOMs. See text for details. See Fig. C.2 for a picture of the lab setup.

In our setup, we have fixed the parameters of the circuit and the AWG for generating about 10 dB of technical noise for an optical power of 400 μW with a duty cycle of the pulses of 1/3.

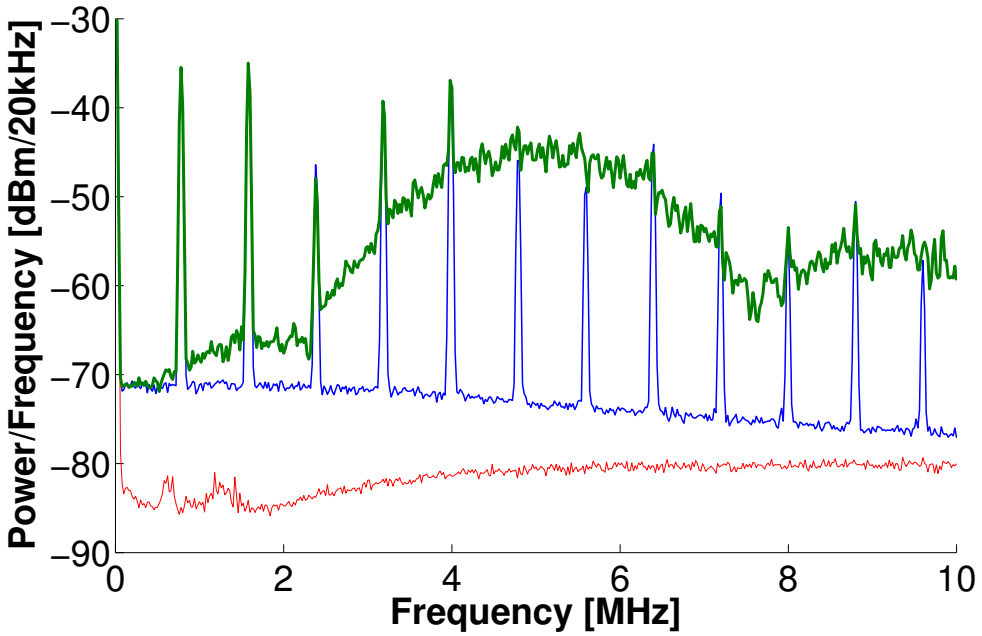

Figure 3.9: Illustration of noise contributions in the power spectrum of a train of pulses. Thin red curve shows the electronic noise of the detector, i.e., with no optical signal introduced. Blue medium curve shows power spectrum with no introduced technical noise. This shows narrow peaks at harmonics of the pulse repetition frequency rising from a shot-noise background. The roll-off in signal strength is due to the 5 MHz bandwidth of the detector. Thick green curve shows power spectrum with an introduced technical noise with central frequency of 5 MHz and FWHM bandwidth of 1 MHz.

3.6 Calculating the optimal pattern function

To measure the noise spectra upon which the pattern function will be based, we use an oscilloscope (Lecroy Wavejet-324), rather than a spectrum analyzer. This allows us to use the same instrument for noise characterization and optimization as we will later use to acquire signals to process by digital filtering.

We collect 5×10^5 samples in a 1000 μs acquisition time containing a total of 800 pulses ~400 ns duration, with a duty cycle of 1/3. For this train of pulses we compute the power spectral density (PSD) for

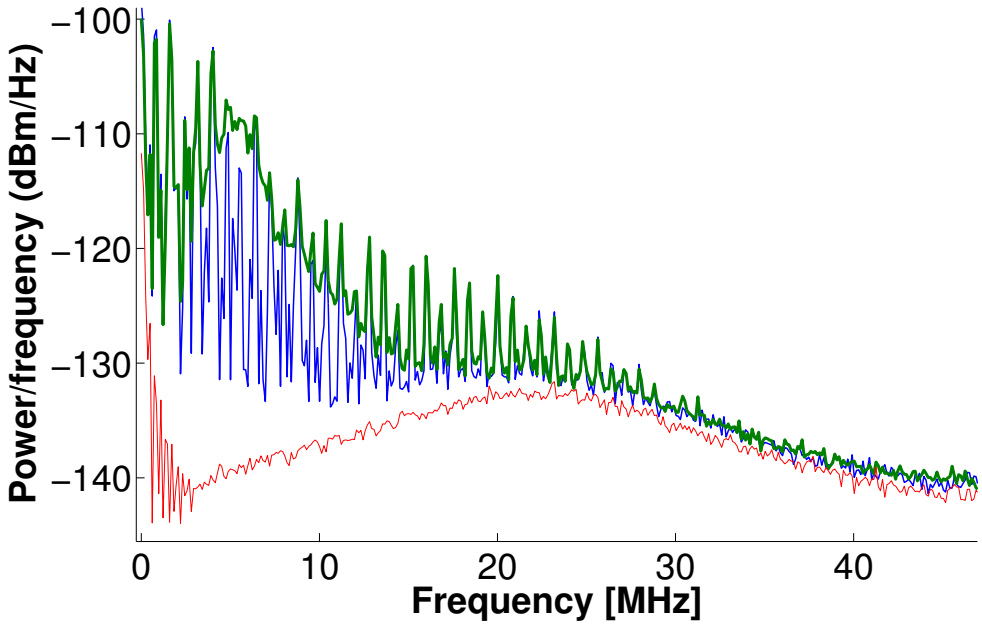

Figure 3.10: Power spectral density from a train of 800 pulses, considering three cases: signal without technical noise (blue line), signal with technical noise (bold green line), and electronic noise (red thin line).

three cases: 1) signal without added technical noise, 2) signal with added technical noise, and 3) the electronic noise. Figure 3.10 shows an example of PSD calculated for these cases. From these PSDs we can then extract the parameters necessary for computing the optimal pattern function, namely electronic background, technical noise power and shot-noise power. Using these parameters, and following the method explained in section 2, we have calculated the optimal pattern function $g(t)$ for different average powers of the beam, from 0 to 400 μW in steps of 20 μW.

3.7 Shot-noise-limited detection with pulses

Because the pulses are non-overlapping, as seen in Fig. 3.5, we can isolate any single pulse by keeping only the signal in a finite window containing the pulse, to get a waveform as illustrated in Fig. 3.11. Also shown there is the optimal pattern function. This illustrates

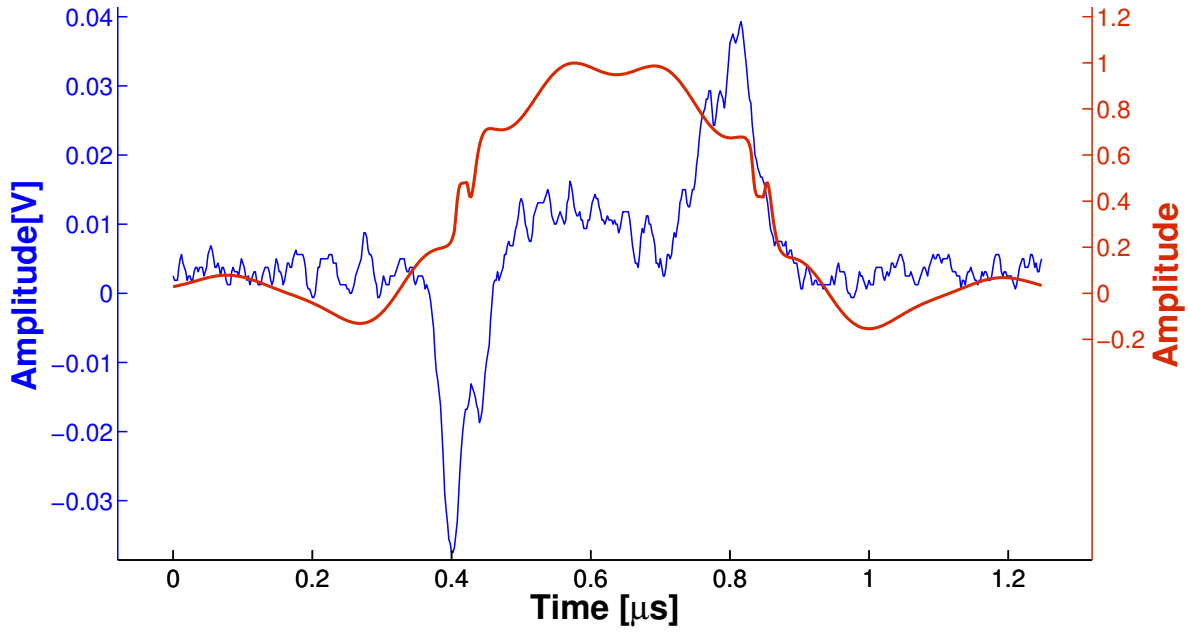

Figure 3.11: Example of cutting of the pulses (blue thin line) and the corresponding pattern function (red thick line).

some qualitative features of the optimal pattern function, which is 1) orthogonal to the residual common-mode signal $h_S * \phi_S$, which first goes negative and then positive, 2) well overlapped with the differential-mode signal $h_D * \phi_D$, which is positive, and 3) smooth with some ringing, to suppress both high-frequency and low-frequency noise.

Definition 3.7.1 (Estimators)
For each pulse we compute the estimators $\hat{S}_{\text{raw}}$, $\hat{S}_{\text{W}}$ and $\hat{S}_{\text{opt}}$, using pattern functions $\gamma(t) = 1$ (raw estimator), $\gamma(t) = w(t)$ (Wiener estimator) and $\gamma(t) = g(t)$ (optimal model-based estimator), respectively.

Definition 3.7.2 (Wiener filter)
The Wiener filter $w(t)$ can be defined as the Fourier transform of the frequency domain representation of the Wiener filter $W(\omega)$, given by the ratio of the cross-power spectrum of the noisy signal with the desired signal over the power spectrum of the noisy signal [21]. For more details see the appendix A.3.

3.7.1 Shot-noise limited detection with pulses

We first show that the system is shot-noise limited in the absence of added technical noise. For this, we compute the variance of $\hat{S}_{\text{raw}}$, this variance is a noise estimation, computed from a pulse train without technical noise, as a function of optical power P. We fit the resulting variances with the quadratic $\text{var}\,(\hat{S}_{\text{raw}}) = A + BP + CP^2$, and obtain $A = (4.5 \pm 0.3) \times 10^{-20} J^2$, $B = (2.4 \pm 0.1) \times 10^{-22} J^2/\mu W$ and $C = (6.7 \pm 0.6) \times 10^{-26} J^2/\mu W^2$. The data and fit are shown in Fig. 3.12(a), and clearly show a linear dependence on P, a hallmark of shot-noise limited performance.

3.7.2 Measuring technical noise with pulses

Now, we proceed as before with the exception that in this case we introduce technical noise to the signal. We obtain the following fitting parameters: $A = (4.5 \pm 0.3) \times 10^{-20} J^2$, $B = (1.9 \pm 0.1) \times 10^{-22} J^2/\mu W$ and $C = (4.12 \pm 0.05) \times 10^{-24} J^2/\mu W^2$.

We observe from Fig. 3.12(b) that the noise estimation for the data that has technical noise exhibits a clearly quadratic trend, in contrast to the linear behavior where no technical noise is introduced. The results shown in Figs. 3.12(a) and 3.12(b) prove that, with our designed system, it is possible to introduce technical noise in a controlled way.

3.8 Filtering 10 dB of technical noise using an optimal pattern function

To illustrate the performance of our technique when filtering technical noise, we introduce a high amount of noise —about 60 dB above the shot noise level at the maximum optical power— to the light pulses produced by the AOMs. After balancing a maximum of 10 dB remains in the electronic output, which is then filtered by means of the optimal pattern function technique.

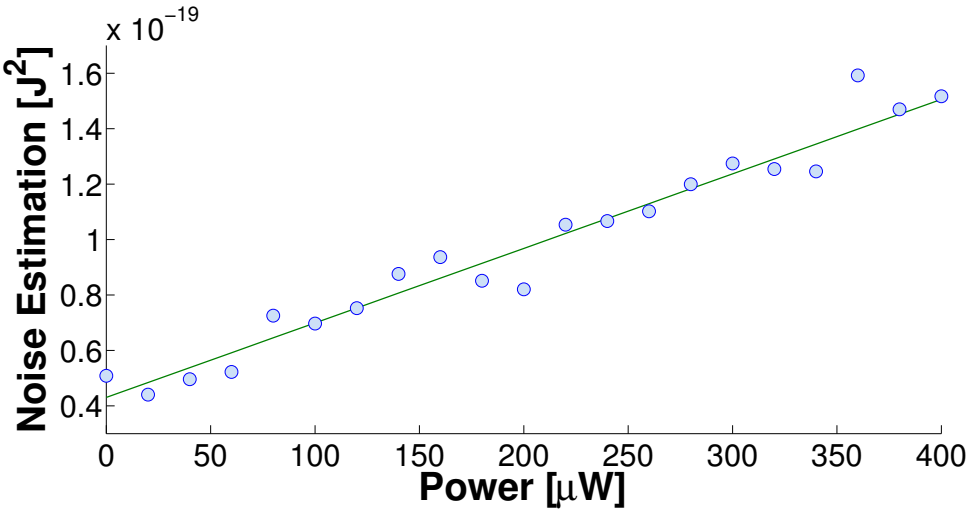

(a)

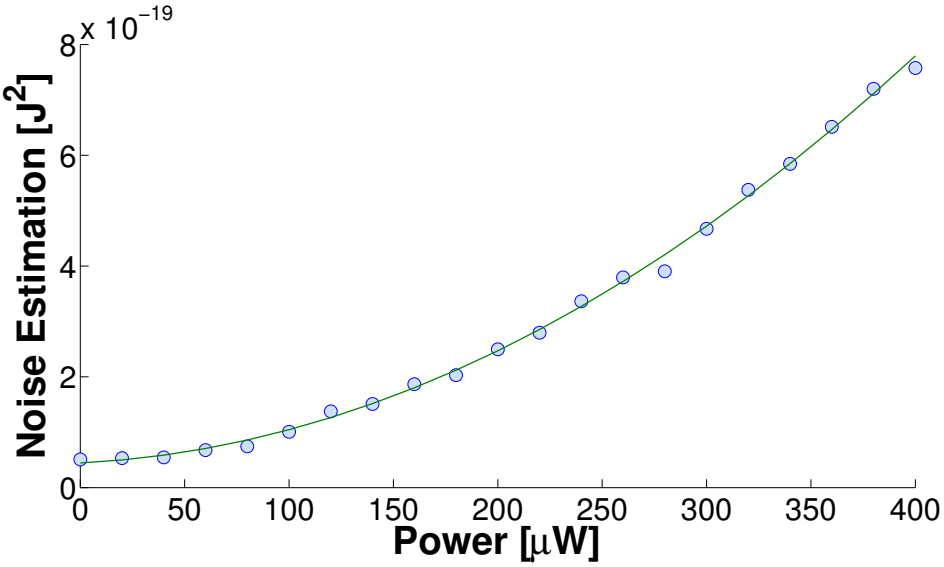

(b)

Figure 3.12: Computed noise estimation as a function of the optical signal power (a) without and (b) with technical noise introduced. Circles: experimental data, solid line: quadratic fit.

We have verified the correct noise filtering by comparing the results with shot-noise limited pulses. For this purpose, we compute var $(\hat{S}_{\text{opt}})$, the variance of the optimal estimator for each power, and for each data set, the shot-noise limited and the noisy one. Figure 3.13 shows the computed noise estimation as function of the optical power for both. Notice that the two noise estimations are linear with the optical power. Moreover, we observe that both curves agree at

$\sim 91 \pm 5\%$, using the ratio of the slopes, which allows us to conclude that, by using this technique, we can retrieve shot-noise limited pulses from signals bearing high amount of technical noise.

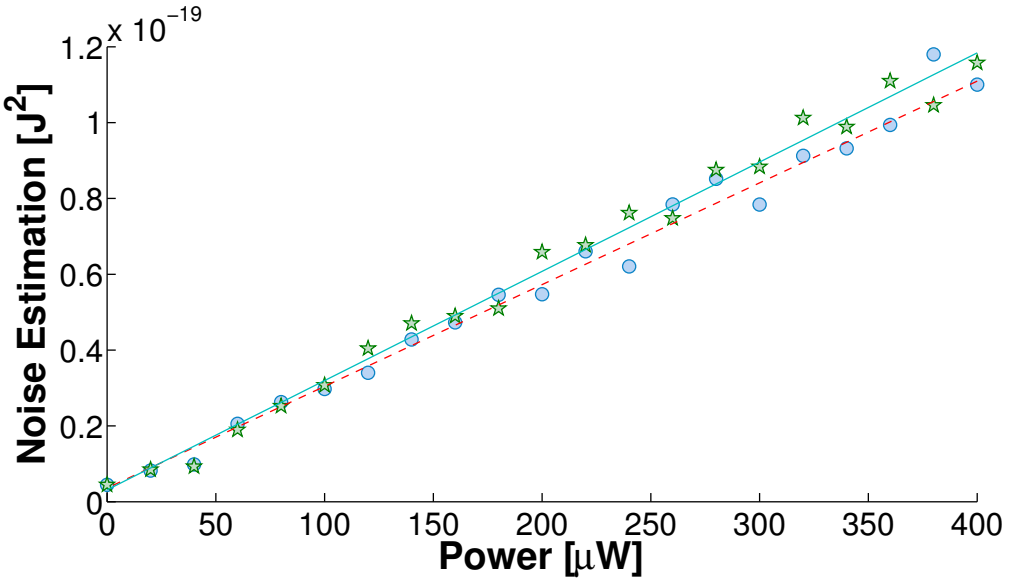

Figure 3.13: Computed noise estimation, using the optimal pattern estimator, as a function of the optical power for shot-noise limited pulses (blue circles) and pulses with technical noise (green stars). Their corresponding quadratic fits are shown in red dashed and cyan lines, respectively.

Chapter 4

Optimal signal recovery for pulsed polarimetry

Optical readout of magnetic atomic ensembles have become the most sensitive instrument on Earth for measuring the magnetic field [11, 12]. Most prominent among the magneto-optical effects are the Faraday and the Voigt effects, which interactions of near-resonant light with the atomic vapor have demonstrated sensitivities better that $1\text{ft}/\sqrt{\text{Hz}}$ [22, 23]. The magnetic field is retrieved monitoring the polarization of the transmitted light beam [10], and when is used a balanced detector for measuring the polarization, the method has intrinsic advantages, in the sense that this configuration can be used to performed shot-noise limited measurements [13, 16], and also has the intrinsic ability to detect very small polarization-rotation angles, see Fig. 4.1. Also Faraday rotation, in the last years, have been used for spectral filtering using several schemes and techniques [24, 25, 26, 27] (the first and the last two references uses Faraday anomalous dispersion optical filter -FADOF-) making relevant to measure with high accurancy those angles.

The pattern function developed in chapter 2 and tested in chapter 3 can also be used for optimally recover the polarization from a pulsed of light. In this chapter, we recall the foundations of the characterization of the polarization state of the light, namely the Stokes parameters —see section 4.1. For a further introduction in

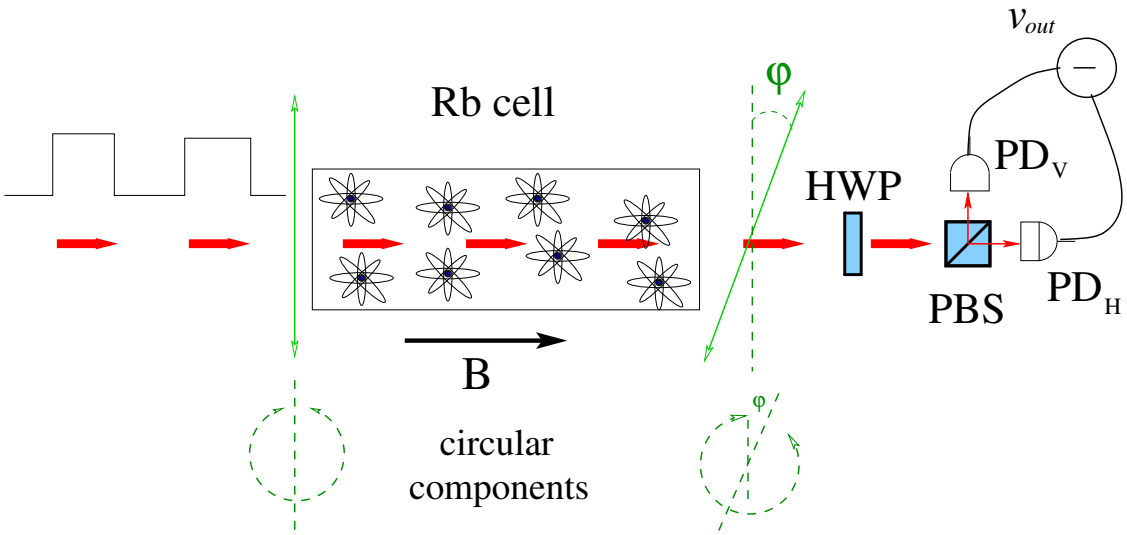

Figure 4.1: The Faraday effect and the balanced detection. Linear polarized light passes through an atomic medium, the circular components of linearly polarized light (equal in amplitude) acquire different phase shifts, leading to a rotation φ of the linearly polarized light. Also, a different in absorption between the components causes ellipticity in the transmitted light beam.

the subject and more details about polarimetry and ellipsometry see [52, 53]. Later, we show how to estimate the polarization state and the polarization-rotation angle —see sections 4.2 and 4.3. Finally, it is calculated the noise angle estimation for the polarization-rotation angle using the pattern function —see section 4.5.

4.1 Stokes parameters

The determination of the polarization state from a light beam can be described in terms of four observables, known as the Stokes parameters. Such parameters describe completely any polarization state of the light. The S_0 parameter expresses the total optical intensity. The S_1, S_2, S_3 parameters describe the polarization state [54, 55].

The same task can be done using pulses of light. In the context of classical optics, it is possible to fully determined the polarization state of a single pulse, for example using the technique of the four-detector

photo-polarimeter [56]. Nevertheless for quantum optics, it is not possible to fully determined the polarization state of a quantum pulse, due to uncertainties and expected values from the Stokes parameters are connected [57, 58, 59, 60, 61].

To measure with high precision the polarization state from a pulse of light can be a critical task [61, 62] that can lead to applications on measuring magnetic fields. Optical magnetometers, based on optical readout of magnetic atomic ensembles, are currently the most sensitive devices [11, 12]. The optical readout is done by a polarimeter that is prepared to measure the rotation angle from a linear polarized beam.

The polarization state of the light can be described using the Stokes parameters, and visualized using the Poincaré Sphere, see Fig. 4.2. It is a set of four parameters $\{S_0, S_1, S_2, S_3\}$ that fully characterizes the polarization state of the light, they were defined by G. G. Stokes in 1852 [54]. They describe the preference of the light for a given polarization:

S_0. Corresponds to the total intensity I or energy density in the light.

S_1. Quantifies how H (linear horizontally polarized light) or V (linear vertically polarized light) is the light,

S_2. Quantifies how 45^0 (linear 45^0 polarized light) or -45^0 (linear -45^0 polarized light),

S_3. Quantifies how R (right circularly polarized light) or L (left circularly polarized light) is the light.

The mathematical description of the Stokes parameters is given by:

$$\begin{aligned} S_0 &\equiv E_H E_H^* + E_V E_V^*, \\ S_1 &\equiv E_H E_H^* - E_V E_V^*, \\ S_2 &\equiv E_H E_V^* - E_H E_V^*, \\ S_3 &\equiv i\left(E_H E_V^* - E_V E_H^*\right). \end{aligned} \tag{4.1}$$

Where E_H and E_V are the complex amplitudes of the electric field $\vec{\mathbf{E}}$ in the polarization basis $(\hat{\epsilon}_H, \hat{\epsilon}_V)$.

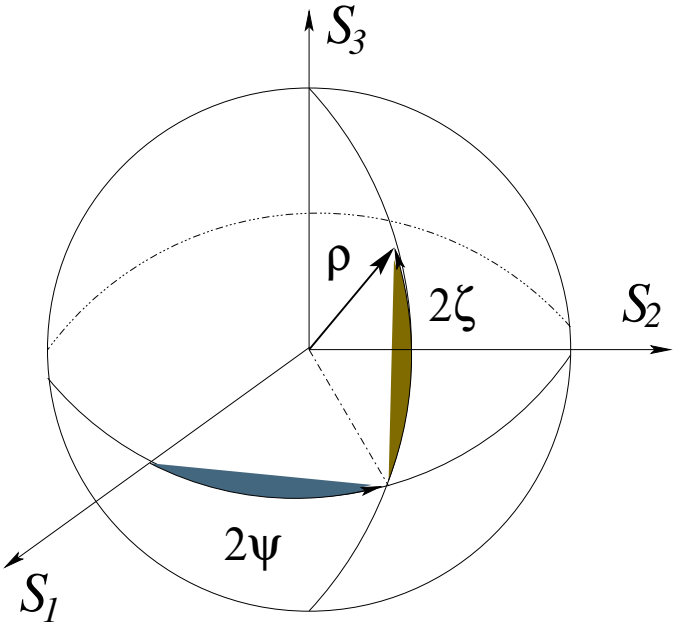

Figure 4.2: Representation of the Stokes parameters in the Poincaré sphere showing the polarized beam defined by the set of coordinates $(\rho, 2\psi, 2\zeta)$.

In the case of fully polarized light S_0 is given by:

$$S_0 = \sqrt{S_1^2 + S_2^2 + S_3^2}. \tag{4.2}$$

The Stokes parameters can be written in spherical coordinates (ρ, ψ, ζ) as follows:

$$\begin{array}{rcl} S_0 & \equiv & \frac{\rho}{\mathcal{P}}, \\ S_1 & \equiv & \rho\cos(2\psi)\cos(2\zeta), \\ S_2 & \equiv & \rho\sin(2\psi)\cos(2\zeta), \\ S_3 & \equiv & \rho\sin(2\zeta). \end{array} \tag{4.3}$$

Where we have introduced the parameter

$$\mathcal{P} = \frac{\sqrt{S_1^2 + S_2^2 + S_3^2}}{S_0}, \tag{4.4}$$

as the degree of polarization. Note that the effective polarization-intensity ρ is written $\rho = \mathcal{P}I$. For a beam that is fully polarized $\rho = I$.

The Stokes parameters, in spherical coordinates, can easily be represented in the Poincaré sphere [55], see Fig. 4.2.

4.2 Estimation of the polarization state

To measure the Stokes parameters is needed an apparatus capable of separating orthogonal pairs of polarizations. It is possible to measure the S_1 and the S_2 using a setup like the one in Fig. 2.1, varying the angle of the half-wave plate.

Fixing the half-wave plate angle-position for retrieving the S_1 Stokes parameters we send a V (linear vertically polarized) pulse followed by a H (linear horizontally polarized) pulse. Measuring the signal depicted in Fig. 4.3.

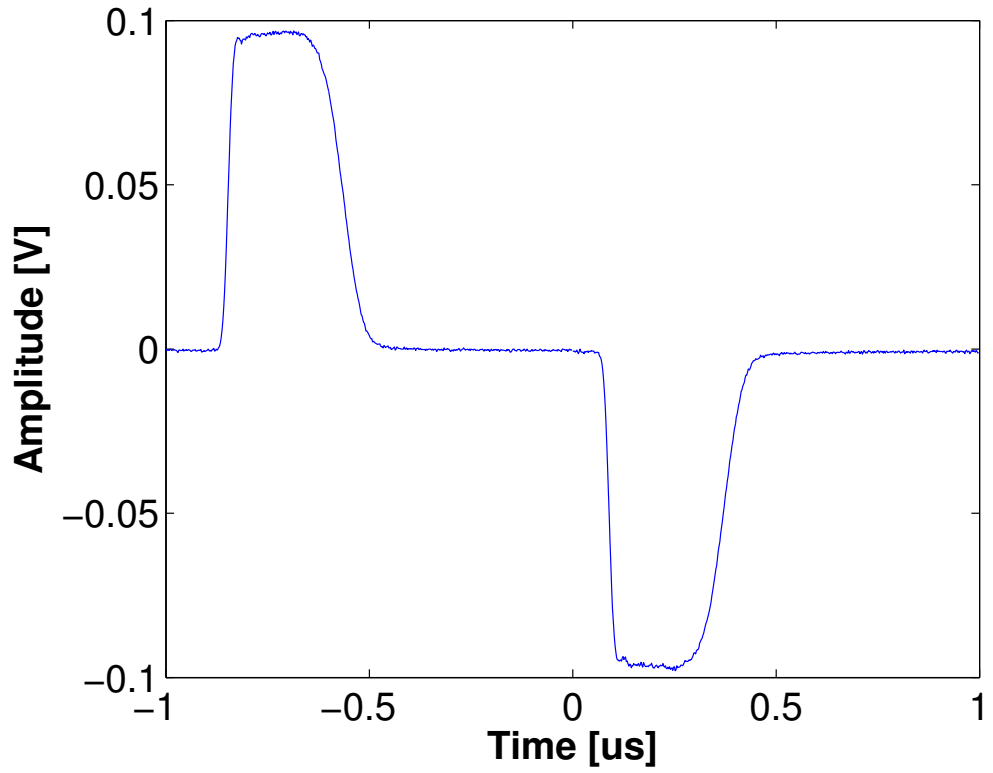

Figure 4.3: Example of linearly polarized pulses seen by the balanced detector. Voltage[V] vs time[μs].

To estimate the polarization state of each pulse is computed its

time integral. Obtaining $e_1 = 0.0268$ for the first pulse and $e_2 = -0.0279$ for the second one, that corresponds to $S_1/S_0 = -0.97$ and $S_1/S_0 = 0.99$ respectively.

4.3 Estimation of the polarization-rotation angle

Now, we focus our attention in estimating the polarization-rotation angle φ from a linear polarized beam, see Fig. 4.1. As a particular case of Eq. (2.1), and introducing the rotation-angle φ explicitly we obtain

$$v_{\text{out}}(t) = h_H * \phi_S \sin^2\left(\frac{\pi}{4} + \varphi\right) - h_V * \phi_S \cos^2\left(\frac{\pi}{4} + \varphi\right) + v_N(t). \tag{4.5}$$

Where for $\varphi = 0$, we have the "balanced condition".

As a further simplification we take $h_H \approx h_V \approx \frac{h_S}{2}$, and neglecting the electronic noise, thus the main component of the signal is

$$v_{\text{out}}(t) \approx \frac{h_S}{2} * \phi_S \sin(2\varphi) \tag{4.6}$$

Remark 4.3.1
The estimators $\hat{S}_{\text{raw}}, \hat{S}_{\text{W}}$ and $\hat{S}_{\text{opt}}$, previously defined in definition 3.7.1 can be approximately calculated using the last expression Eq. (4.6) as electronic output. Also is a good approximation to calculate the derivative of the estimator with respect to the rotation-angle $(\frac{d\hat{S}}{d\varphi})$ using Eq. (4.6), although for a computer is the same to calculate the derivative of the full expression in Eq. (4.5).

4.4 Wiener estimator

In order to apply the Wiener filter it is needed to construct and ideal version of the signal or the desired signal, according to the definition of the Wiener filter, see in definition 3.7.2.

In order to create the ideal signal we take the model of the impulse response functions in Eq. (3.3), together with the model of the output voltage in Eq. (2.1) without electronic noise, this lead us to an expression of the idealized signal. Then we can compute the Wiener filter for each signal, and in such way obtaining the Wiener estimator, see **definition** 3.7.1. The details for computing the Wiener filter are found in the book of Saeed Vaseghi [21], a short description is presented in the appendix A.3.

In Fig. 4.4(a) is shown the idealized signal, together with a signal with no technical noise, in Fig. 4.4(b) we have a signal that has a couple of dBs of technical noise and together with the one that is Wiener-filtered.

4.5 Optimal estimation of the polarization-rotation angle

The experimental setup that we have implemented, see Fig. 2.1, can perform also as a pulsed signal polarimeter. For instance, it is possible to determine a small polarization-rotation angle φ from a 45° linear polarized light pulse. Along these lines, we make use of three estimators $\hat{S}_{\text{raw}}, \hat{S}_{\text{W}}$ and $\hat{S}_{\text{opt}}$ to determine the amount of noise on the estimation of the polarization-rotation angle. From the obtained results, we show that the model-based estimator outperforms the other two.

We proceed to calculate the noise on the polarization-rotation angle φ estimation, for this determination we calculate the variance of φ. We notice that the Taylor approximation of the variance of $\hat{S}(\varphi)$ is

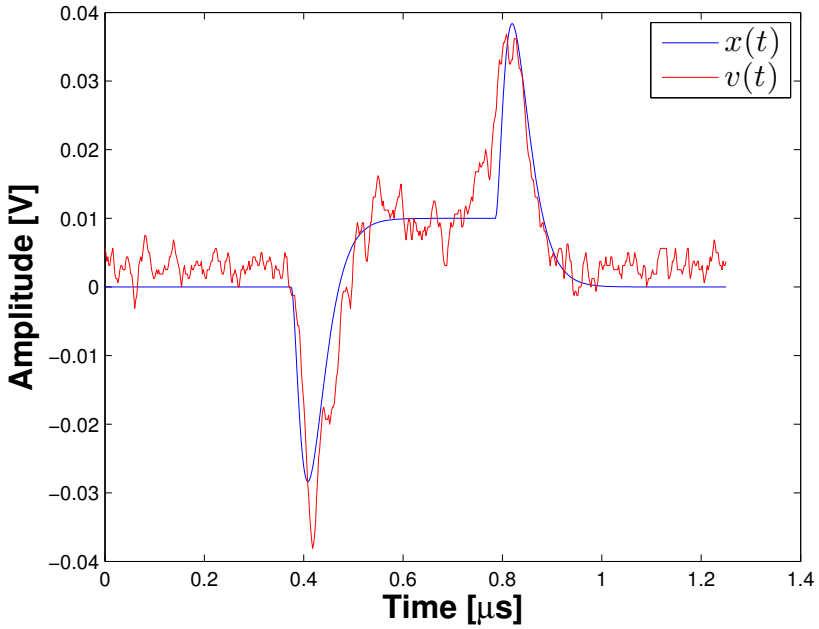

(a)

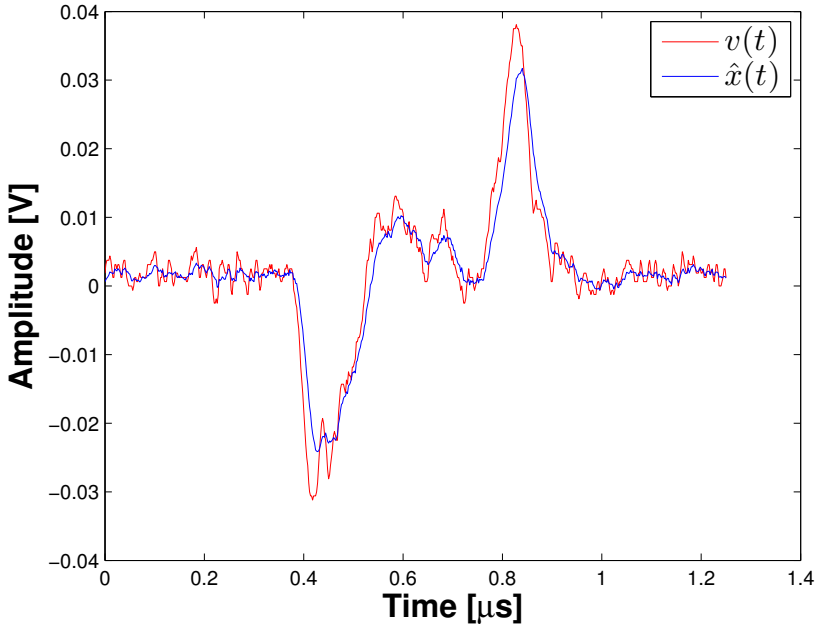

(b)

Figure 4.4: Wiener filtering of pulses of light. (a) Construction of the ideal signal from a pulse that has not technical noise, (b) Wiener-filtered pulse from one that has a couple of dBs of technical noise.

$$\mathrm{var}\,(\hat{S}) \approx \left(\frac{d\hat{S}}{d\varphi}\right)^2 \mathrm{var}\,(\varphi). \tag{4.7}$$

For small angles φ, the function $\hat{S}(\varphi)$ is approximately linear on φ, so the contribution from higher order terms can be disregarded.

Therefore, the noise on the angle estimation is

$$\text{var}\,(\varphi) = \frac{\text{var}\,(\hat{S})}{\left(\frac{d\hat{S}}{d\varphi}\right)^2}. \tag{4.8}$$

We can then compute this expression using the three before mentioned estimators. For such task we use the experimental data together with an analytical approximation of the derivative, that takes as input the measured data, see the remark 4.3.1 for details. Figure 4.5 depicts the noise angle estimation, showing that the optimal pattern function performs better than the other estimators when eliminating the technical noise and reducing the electronic noise. In particular, the based-model estimator surpasses the Wiener estimator, which is a widely used method in signal processing [21].

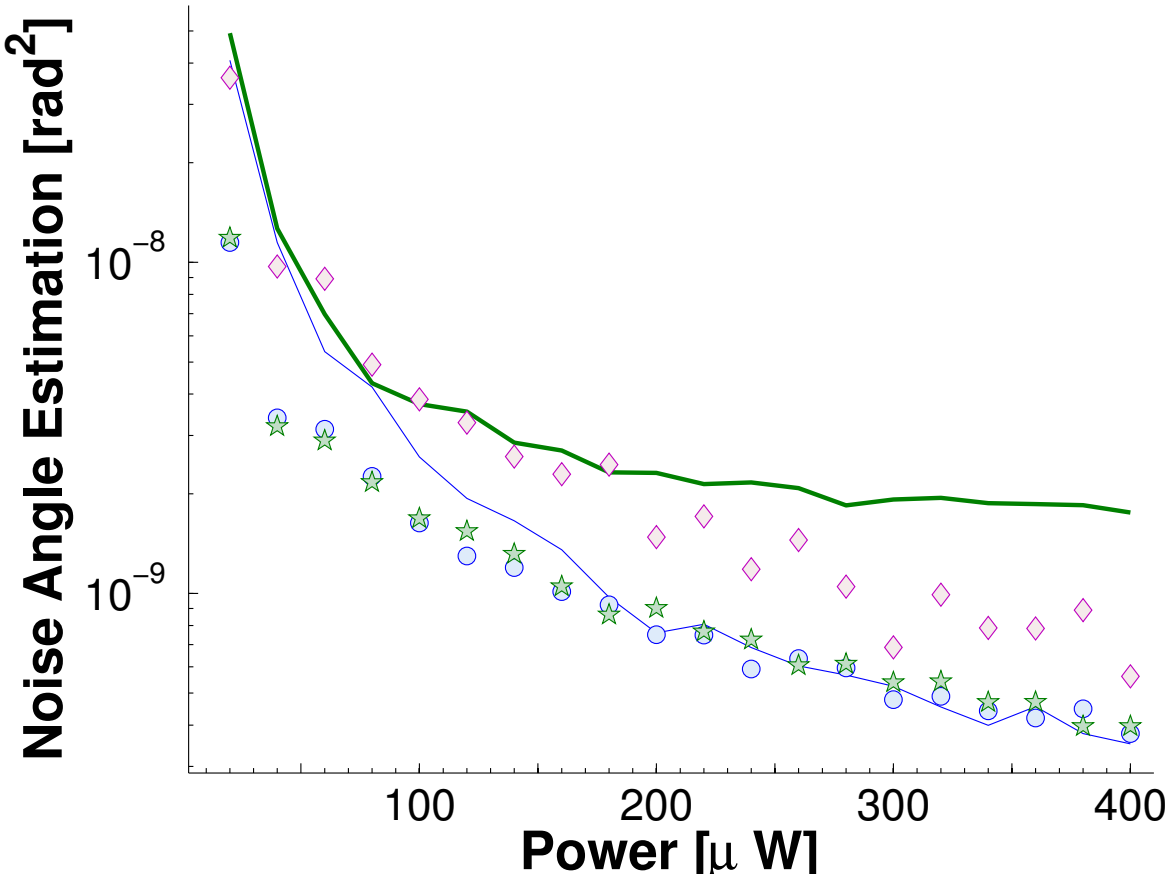

Figure 4.5: Noise angle estimation as a function on the optical power. Raw estimators with technical noise (green bold line) and without (blue medium line). Wiener estimator with technical noise (pink diamonds). Model-based estimators with technical noise (green stars) and without (blue circles). For the sake of visualization the results are presented in a semi-log graph.

Chapter 5

Conclusions

We have studied in theory and with an experimental demonstration, the optimal recovery of light pulses via balanced detection. We developed a theoretical model for a balanced detector and the noise related to the detection of optical pulses. We minimized the technical and electronic noise contributions obtaining the optimal (model-based) pattern function. We designed and implemented an experimental setup to test the introduced theoretical model. In this experimental setup, we produced technical noise in a controlled way, and retrieved shot-noise limited signals from signals bearing about 10 dB of technical noise after balanced detection. Finally, we compare against naïve and Wiener filter estimation for measuring rotation angles, and confirm superior performance of the model-based estimator.

The results presented here might lead to a better polarization-rotation angle estimations when using pulses leading to probe magnetic atomic ensembles in environments with technical noise [15, 63]. This possibility is especially attractive for balanced detection of sub-shot-noise pulses [6, 13], for which the acceptable noise levels are still lower.

5.1 Outlook

The first application that we had in mind from the beginning of the project is to combine the theory and the calculation procedure for estimate the noise of the pulses of light for producing *Pulsed Polarization Squeezing,* see more details in the appendix A.4. It is possible to produce squeezing using the techniques that were developed here using the setup shown in Fig. 5.1.

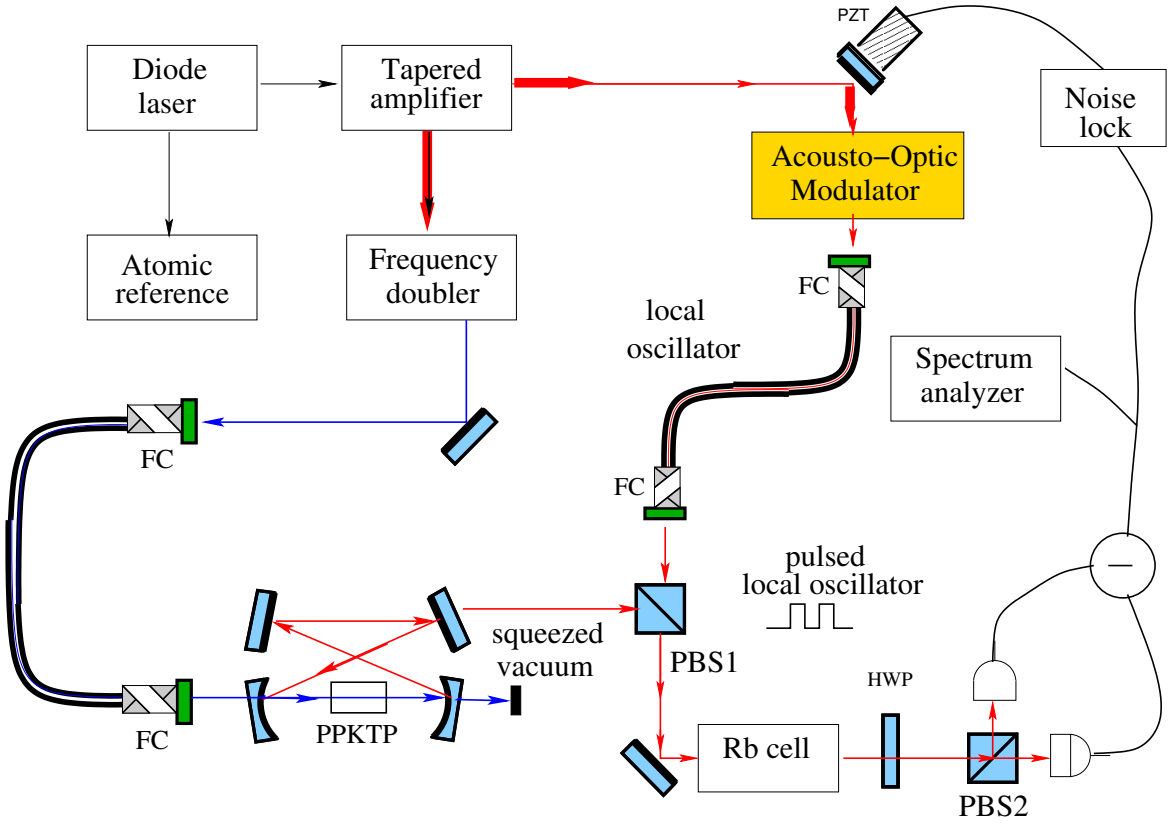

Figure 5.1: Production of pulsed polarization squeezing.

The setup, and all the characterization procedures are ready to undertake this task, the only negative input is that our optical parametric oscillator (OPO) that produces the polarization squeezing is a little degraded from its initial state, as a normal consequence of aging.

At this time, several tasks have been planned for improving again the production of squeezing and so, in the near future produce pulsed polarization squeezing with a good degree of squeezing.

The other in house application will be magnetic field estimation using pulses of light that can be undertaken by Vito-Giovanni Lucivero another PhD student that was working with me in the experimental realization of the present project.

The setup of two acousto-optic modulators is currently used by Federica Beduini because of the high extinction ratio higher that 1×10^{-7} that we can obtain from the pulses on and off, see section 3.1. She is using the setup for an experiment on "entanglement and squeezing".

The knowledge obtained programing the arbitrary waveform generator will be available for other members of the group, but also is now spreading on other experimental groups. Since the production of noise, even if is not perfect, has several applications for testing prototypes and proof-of-principle experiments.

Appendix A

Background Information and detail calculations

A.1 Signal processing methods

From the book of Saeed Vaseghi [21].

> A signal can be defined as the variation of a quantity by which information is conveyed regarding the state, the characteristics, the composition, the trajectory, the course of action or the intention of the signal source: *"A signal is a means to convey information"*.

The need of extracting a piece of information from a weak or noisy or complex signal have created the field of: *signal processing theory.* Signal processing methods have evolved in algorithmic complexity aiming for optimal utilization of the information in order to achieve the best performance. In general the computational requirement of signal processing methods increases, often exponentially, with the algorithmic complexity. Depending on the method used, digital signal processing algorithms can be categorized into one or a combination of four broad categories. These are non-parametric signal processing,

model-based signal processing, Bayesian statistical signal processing and neural networks.

Non-parametric methods. As the name suggests, they do not use a parametric model. They process the signal as a whole waveform or sequence. As a drawback, these methods do not use any parametric form of the signal so they do not take advantage of this information.

Model-based methods. These methods uses the structures on the signals to process them. As a drawback, these methods process badly a signal that do not fulfill the pattern or the structure that was assumed.

Bayesian statistical methods. These methods are based on Bayesian interference theory, see [21] for more information.

Neural networks. These methods resemble the biological neurons, where each neuron can perform a simple task, but the processing of the signal is done by the network, where several neurons, interconnected and with a hierarchically structured, process the signal.

A.2 Parseval's theorem and Wiener-Khinchin's theorem

THEOREM A.2.1 (PARSEVAL'S THEOREM)
Let $F(\omega)$ and $G(\omega)$ be the Fourier transform of $f(t)$ and $g(t)$, respectively. Then

$$\begin{aligned}
\int_{-\infty}^{\infty} f(t)\bar{g}(t)dt &= \int_{-\infty}^{\infty}\left[\int_{-\infty}^{\infty} F(\omega)e^{2\pi \mathbf{i}\omega t}d\omega\right]\left[\int_{-\infty}^{\infty}\overline{G}(\omega')e^{-2\pi \mathbf{i}\omega' t}d\omega'\right]dt,\\
&= \int_{-\infty}^{\infty} F(\omega)\int_{-\infty}^{\infty}\overline{G}(\omega')\left[\int_{-\infty}^{\infty} e^{2\pi \mathbf{i}t(\omega-\omega')}dt\right]d\omega' d\omega.\\
&= \int_{-\infty}^{\infty} F(\omega)\left[\int_{-\infty}^{\infty}\overline{G}(\omega')\delta(\omega-\omega')d\omega'\right]d\omega,\\
&= \int_{-\infty}^{\infty} F(\omega)\overline{G}(\omega)d\omega.\blacksquare
\end{aligned}$$

We can show a partial demonstration of the Wiener-Khinchin's theorem that states that the Fourier transform of the auto-correlation function is the power spectral density of the process. The Wiener-Khinchin theorem is proved using stochastic processes [64], here we will prove the particular case of deterministic functions.

From the definition of the Fourier Transform we find that:

$$\begin{aligned}\int_{-\infty}^{\infty}|F(w)|^2dt &= \left[\int_{-\infty}^{\infty}f(t)e^{2\pi\mathbf{i}\omega t}dt\right]\left[\int_{-\infty}^{\infty}f(t)e^{-2\pi\mathbf{i}\omega t}dt\right], \\ &= \int_{-\infty}^{\infty}\left(\int_{-\infty}^{\infty}f(t)f(t+\tau)dt\right)e^{-2\pi\mathbf{i}\omega\tau}d\tau. \\ &= \int_{-\infty}^{\infty}h(t,\tau)e^{-2\pi\mathbf{i}\omega\tau}d\tau.\blacksquare\end{aligned}$$

For obtaining the second line we made the transformation $t \to t+\tau$, we have defined implicitly the auto-correlation function for deterministic signals.

$$h(t,\tau) = \int_{-\infty}^{\infty}f(t)f(t+\tau)dt. \tag{A.1}$$

We want to clarify some potential confusions, PSDs can be specified as *one-sided* functions of only positive frequencies, or as (two times smaller) *two-sided* functions of positive and negative frequencies. Noise PSDs are mostly one-sided in the engineering disciplines, since we measure them using an electronic spectrum analyzer, but often two-sided in physics and in maths, since we obtain them using the Fourier transform. But having this clarification in mind it is easy to make theory and experimental data compatible.

A.3 Wiener filter estimator

The Wiener filter estimator $\hat{S}_{\mathrm{W}}$ can be derived from the frequency domain Wiener filter output $\hat{X}(\omega)$ [21] define as

$$\hat{X}(\omega) \equiv W(\omega)V(\omega), \tag{A.2}$$

where $W(\omega)$ and $V(\omega)$ are the Wiener filter and the electronic output in frequency domain, respectively.

We define $W'(\omega) \equiv W^*(\omega)$ and $w'(t) \equiv w^*(t)$ and make use of the inner product of the Parseval's theorem (see theorem A.2.1), see Eq. (2.12)

$$\int_{-\infty}^{\infty} W'(\omega)V_{\text{out}}(\omega)d\omega = \int_{-\infty}^{\infty} w'(t)v_{\text{out}}(t)dt. \tag{A.3}$$

Then the Wiener filter estimator $\hat{S}_{\text{W}}$ is $\int_{-\infty}^{\infty} w'(t)v_{\text{out}}(t)dt$ corresponding to Eq. (2.4) for $\gamma(t) = w'(t)$.

The Wiener filter $W(\omega)$ is

$$W(\omega) = \frac{\langle |V^*_{\text{ideal}}(\omega)V_{\text{out}}(\omega)| \rangle}{\langle |V_{\text{out}}(\omega)|^2 \rangle}. \tag{A.4}$$

In order to compute the Wiener filter it is necessary to construct the ideal signal $V_{\text{ideal}}(\omega)$, a signal without all noise contributions.

A.4 Theory of pulsed polarization squeezing

In this section, it is characterized some features of "pulsed polarization squeezing". We show a formal proof that a state with zero average field and quadrature squeezing, when is combined with a strong coherent state of the orthogonal polarization, quantum features of the quadrature variables are transferred onto the polarization variables. Obtaining in this way, that each pulse satisfies the definition of polarization squeezing.

Firstly, we need the definitions of *quadrature operators*, *quadrature squeezing*, *Stokes operators*, and *the generalized uncertainty principle*

to motivate the definition of *polarization squeezed state*. Secondly, the commutator relations, and a way to split the operator into "classical amplitude" plus a "noise operator".

Definition A.4.1 (Quadrature operators)
The quadrature operators ($\hat{X}_j^+$, $\hat{X}_j^-$) of mode j, in terms of the creation $\hat{a}_j^\dagger$ and annihilation $\hat{a}_j$ ($\hat{a}_j$ and $\hat{a}_j^\dagger$ satisfy the commutation relations $[\hat{a}_j, \hat{a}_k^\dagger] = \delta_{jk}$, $[\hat{a}_j^\dagger, \hat{a}_k^\dagger] = 0$, $[\hat{a}_j, \hat{a}_k] = 0$) are

$$\hat{X}_j^+ \equiv \hat{a}_j^\dagger + \hat{a}_j, \quad \hat{X}_j^- \equiv i(\hat{a}_j^\dagger - \hat{a}_j), \quad j = x, y. \tag{A.5}$$

The generalized quadrature operator is:

$$X_j(\theta) \equiv X_j^+ \cos\theta + X_j^- \sin\theta. \tag{A.6}$$

Remark A.4.1
The commutation relation of the quadrature operators ($\hat{X}_j^+$, $\hat{X}_k^-$) is

$$[\hat{X}_j^+, \hat{X}_k^-] = 2i\delta_{jk}. \tag{A.7}$$

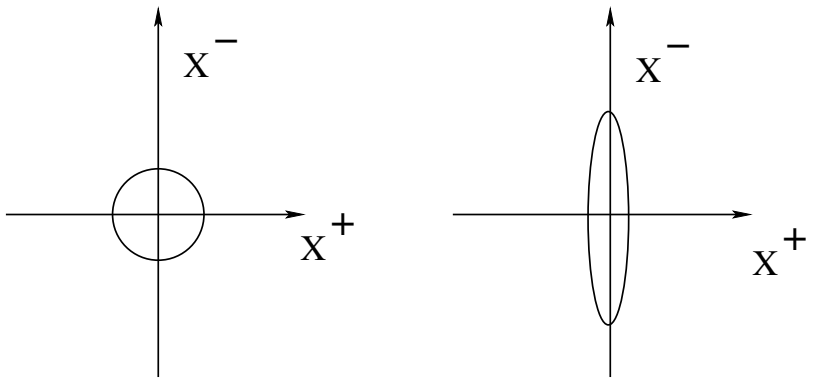

Figure A.1: Example of Quadrature Squeezing. Uncertainty circle/ellipse for (a) coherent state (output from a standard laser) and (b) squeezed state (output from the OPO).

Definition A.4.2 (Quadrature squeezing)
Quadrature squeezing means that the level of quantum fluctuations of one quadrature component (X^+ or X^-) is less than level corresponding to the coherent state ($V_{X^+} = V_{X^-} = 1$), see Fig. A.1. Mathematically

$$V_{X^+} < 1 \quad \text{or} \quad V_{X^-} < 1. \tag{A.8}$$

Where V_A is the variance of the operator A defined by

$$V_A \equiv \langle(\Delta\hat{A})^2\rangle \equiv \langle\hat{A}^2\rangle - \langle\hat{A}\rangle^2. \tag{A.9}$$

And finally $\hat{X}^+$, $\hat{X}^-$ are the quadrature operators, see **definition** A.4.1 for details.

In order to produce polarization squeezing we combine the pulsed local oscillator and the quadrature squeezed in a polarization beam splitter (PBS), see Fig. 5.1. The **Stokes operators** describe the polarization state after the PBS, written in terms of the creation $\hat{a}^\dagger_{x/y}$ and annihilation $\hat{a}_{x/y}$ operators of two orthogonal modes x and y.

$$\begin{aligned}
\hat{S}_0 &\equiv \hat{a}^\dagger_x\hat{a}_x + \hat{a}^\dagger_y\hat{a}_y, \\
\hat{S}_1 &\equiv \hat{a}^\dagger_x\hat{a}_x - \hat{a}^\dagger_y\hat{a}_y, \\
\hat{S}_2 &\equiv \hat{a}^\dagger_x\hat{a}_y + \hat{a}^\dagger_y\hat{a}_x, \\
\hat{S}_3 &\equiv i\big(\hat{a}^\dagger_y\hat{a}_x - \hat{a}^\dagger_x\hat{a}_y\big).
\end{aligned} \tag{A.10}$$

The $\hat{S}_0$ corresponds to the total coherent excitation, whilst the others describe the polarization state. The $\hat{S}_0$ operator commutes with the others: $[\hat{S}_0, \hat{S}_j] = 0, \quad j = 1, 2, 3$, whereas the remaining operators satisfy the commutator:

$$[\hat{S}_1, \hat{S}_2] = 2i\hat{S}_3, \tag{A.11}$$

and the cyclic ones thereof.

Theorem A.4.1 (The generalized uncertainty principle) *If two operators $\hat{A}$ and $\hat{B}$ satisfy the commutation relation $[\hat{A}, \hat{B}] = i\hat{C}$, it follows that*

$$V_A V_B \geq \frac{1}{4}|\langle C\rangle|^2. \tag{A.12}$$

The commutator Eq. (A.11) leads (from the theorem A.4.1) to a restriction on the means and variances by uncertainty relations.

$$V_1V_2 \geq |\langle\hat{S}_3\rangle|^2, \quad V_3V_1 \geq |\langle\hat{S}_2\rangle|^2, \quad V_2V_3 \geq |\langle\hat{S}_1\rangle|^2. \tag{A.13}$$

Where $V_j \equiv V_{S_j}$ and V_{S_j} is defined in Eq. (A.9). This give rise to the formal definition of a polarization squeezed state, in analogy to **definition** A.4.2.

Definition A.4.3 (Polarization squeezed state)
A state is called *polarization squeezed* if

$$V_j < |\langle \hat{S}_k \rangle|, \quad j \neq k. \tag{A.14}$$

An intuitive definition of a polarization squeezed state is a quantum state of light in which the level of quantum fluctuations of one Stokes operator lies below the level corresponding to the coherent polarization state.

The quantum description of the output of an Acousto-Optic Modulator (AOM) is similar to the description of a Beam Splitter (BS). We have that the x-mode (horizontally polarized mode) in the Fig. 5.1 is

$$\hat{a}_x(t) = R(t)\hat{a}_1 + T(t)\hat{a}_\mathrm{v}. \tag{A.15}$$

Where the 1-mode is a coherent state and the v-mode is a vacuum state, $R(t)$ and $T(t)$ are the reflectance and the transmittance that must satisfy the following relations: $|R|^2 + |T|^2 = 1$, and $R^*T - RT^* = 0$, in order to satisfy the commutation relations.

We can write $\hat{a}_j$ as **classical amplitude** or **coherent excitation** α_j plus the **noise operator** $\delta\hat{a}_j$. We can observe that $\langle \alpha_j | \delta\hat{a}_j | \alpha_j \rangle = 0$. In this notation $\hat{a}_1 = \alpha_1 + \delta\hat{a}_1$ and $\hat{a}_\mathrm{v} = \delta\hat{a}_\mathrm{v}$. The y-mode (vertically polarized mode) $\hat{a}_y$ will be $\lim_{\alpha_2 \to 0} \alpha_2 + \delta\hat{a}_2$.

In this notation with $R \equiv R(t)$ and $T \equiv T(t)$, the Stokes parameters become:

$$\begin{aligned}
\hat{S}_0 &= R^2\alpha_1^2 + \alpha_2^2 + R^2\alpha_1\delta X_1^+ + \alpha_2\delta X_2^+ + \alpha_1 RT\delta X_{\mathrm{v}}^+, \\
\hat{S}_1 &= R^2\alpha_1^2 - \alpha_2^2 + R^2\alpha_1\delta X_1^+ - \alpha_2\delta X_2^+ + \alpha_1 RT\delta X_{\mathrm{v}}^+, \\
\hat{S}_2 &= 2R\alpha_1\alpha_2\cos\phi + \alpha_1 R\delta X_2(-\phi) + \alpha_2(T\delta X_{\mathrm{v}}(\phi) + R\delta X_1(\phi)), \\
\hat{S}_3 &= 2R\alpha_1\alpha_2\sin\phi + \alpha_1 R\delta X_2(\tfrac{\pi}{2} - \phi) + \alpha_2(T\delta X_{\mathrm{v}}(\phi - \tfrac{\pi}{2}) + R\delta X_1(\phi - \tfrac{\pi}{2})).
\end{aligned} \tag{A.16}$$

Where $\delta\hat{X}_j^+ \equiv \delta\hat{a}_j^\dagger + \delta\hat{a}_j$, $\delta\hat{X}_j^- \equiv i(\delta\hat{a}_j^\dagger - \delta\hat{a}_j)$ are the quadrature-noise operators, and the generalized quadrature-noise operator is $\delta X_j(\theta) \equiv \delta X_j^+\cos\theta + \delta X_j^-\sin\theta$.

The mean values of Eq. (A.16) are:

$$\begin{aligned}
\langle\hat{S}_0\rangle = \alpha_1^2R^2 + \alpha_2^2, \quad \langle\hat{S}_1\rangle = \alpha_1^2R^2 - \alpha_2^2, \\
\langle\hat{S}_2\rangle = 2R\alpha_1\alpha_2\cos\phi, \quad \langle\hat{S}_3\rangle = 2R\alpha_1\alpha_2\sin\phi.
\end{aligned} \tag{A.17}$$

From Eq. (A.16), we compute the variances of the Stokes parameters.

$$\begin{aligned}
V_0 &= \alpha_1^2R^4\langle(\delta X_1^+)^2\rangle + \alpha_2^2\langle(\delta X_2^+)^2\rangle + \alpha_1^2(RT)^2\langle(\delta X_{\mathrm{v}}^+)^2\rangle, \\
V_1 &= \alpha_1^2R^4\langle(\delta X_1^+)^2\rangle + \alpha_2^2\langle(\delta X_2^+)^2\rangle + \alpha_1^2(RT)^2\langle(\delta X_{\mathrm{v}}^+)^2\rangle, \\
V_2 &= \alpha_1^2R^2\langle(\delta X_2(-\phi))^2\rangle + \alpha_2^2T^2\langle(\delta X_{\mathrm{v}}(\phi))^2\rangle + \alpha_2^2R^2\langle(\delta X_1(\phi))^2\rangle, \\
V_3 &= \alpha_1^2R^2\langle(\delta X_2(\tfrac{\pi}{2} - \phi))^2\rangle + \alpha_2^2T^2\langle(\delta X_{\mathrm{v}}(\phi - \tfrac{\pi}{2}))^2\rangle + \alpha_2^2R^2\langle(\delta X_1(\phi - \tfrac{\pi}{2}))^2\rangle.
\end{aligned} \tag{A.18}$$

For the case $\phi = 0$ they become

$$\begin{aligned} V_0 &= \alpha_1^2 R^4 V_{\delta X_1^+} + \alpha_2^2 V_{\delta X_2^+} + \alpha_1^2 (TR)^2 V_{\delta X_v^+}, \\ V_1 &= \alpha_1^2 R^4 V_{\delta X_1^+} + \alpha_2^2 V_{\delta X_2^+} + \alpha_1^2 (TR)^2 V_{\delta X_v^+}, \\ V_2 &= \alpha_1^2 R^2 V_{\delta X_2^+} + \alpha_2^2 T^2 V_{\delta X_v^+} + \alpha_2^2 R^2 V_{\delta X_1^+}, \\ V_3 &= \alpha_1^2 R^2 V_{\delta X_2^-} + \alpha_2^2 T^2 V_{\delta X_v^-} + \alpha_2^2 R^2 V_{\delta X_1^-}. \end{aligned} \tag{A.19}$$

Where $V_{\delta \hat{X}_j^{+/-}}$ is (the variance) $\langle (\delta \hat{X}_j^{+/-})^2 \rangle - \langle \delta \hat{X}_j^{+/-} \rangle^2 = \langle (\delta \hat{X}_j^{+/-})^2 \rangle$.

The v-mode and 1-mode are vacuum and coherent states, respectively, then $V_{\delta \hat{X}_1^+} = V_{\delta \hat{X}_1^-} = V_{\delta \hat{X}_v^+} = V_{\delta \hat{X}_v^-} = 1$. The 2-mode is a quadrature squeezed state $V_{\delta \hat{X}_2^+} < 1$, $V_{\delta \hat{X}_2^-} > 1$.

$$\begin{aligned} V_0 &= \alpha_1^2 R^2 + \alpha_2^2 V_{\delta X_2^+}, \\ V_1 &= \alpha_1^2 R^2 + \alpha_2^2 V_{\delta X_2^+}, \\ V_2 &= \alpha_1^2 R^2 V_{\delta X_2^+} + \alpha_2^2. \\ V_3 &= \alpha_1^2 R^2 V_{\delta X_2^-} + \alpha_2^2. \end{aligned} \tag{A.20}$$

Finally, using Eqs. (A.17) and (A.20), and $\lim_{\alpha_2 \to 0}$ we can satisfy definition A.4.3 ($V_2 < |\langle S_1 \rangle|$) as

$$\begin{array}{ccc} \lim_{\alpha_2 \to 0}(\alpha_1^2 R^2 V_{\delta X_2^+} + \alpha_2^2) & < & \lim_{\alpha_2 \to 0}(\alpha_1^2 R^2 - \alpha_2^2) \\ \alpha_1^2 R^2 V_{\delta X_2^+} & < & \alpha_1^2 R^2 \end{array} \tag{A.21}$$

Whenever $R(t) \neq 0$, because $V_{\delta \hat{X}_2^+} < 1$. ■

Appendix B

Introducing functions into the Arbitrary Waveform Generator (AWG)

The Arbitrary Waveform Generator can produce, in time domain, any waveform with some limitations. The model TGA1242 has a maximum frequency of 40 MHz. And this gives at the same time the minimum time interval:

$$\Delta t = \frac{1}{40\ MHz}. \tag{B.1}$$

Another important parameter is the number of points $Npoints$ that will have the arbitrary waveform, we observed that is better to give numbers that are a power of two: $Npoints = 2^n$. Typically, we used 2048 or 4096 points.

We design the waveform in the frequency space, and we inverse Fourier transform for obtaining the time-domain sequence. Both in frequency space and in time domain we use the same $Npoints$, for a reasonable definition of the functions it is needed to use at least 1024 points, but is better to use 4096 points. We do not see an substantial improvement putting more points.

We prepare the obtained values as input for a LabView program that helps to transfer the values to the AWG. The values should be prepared as follows: the minimum value inside the AWG is "0", and this corresponds to -1, the maximum inside the AWG is "4096", and this corresponds to 1. We prepare all this using a Mathematica program called *Arbitrary Function Production.nb*, that was develop by us.[1]

We introduce the obtained values using the "GPIB port" of the AWG, and a computer in which we have installed LabView and the GPIB card. We used the LabView program (project): *tga1240.llb* for transferring the values to the AWG. For doing the transfer, after opening the LabView project, one needs to open the subprogram test tga 1240 driver.vi, and later initialize the program. Be sure to have in both, the AWG and the subprogram, the same address for the GPIB port. Using this program one should create blank arbitrary functions with the name and the corresponding number of points. Next, one need to open the subprogram tga ARBITRARYINPUT.vi, using this program one can read the output of the Mathematica program and introduce the values into the AWG.

[1] ArbitraryNoiseProduction.nb also works

Appendix C

Experimental setup in the lab

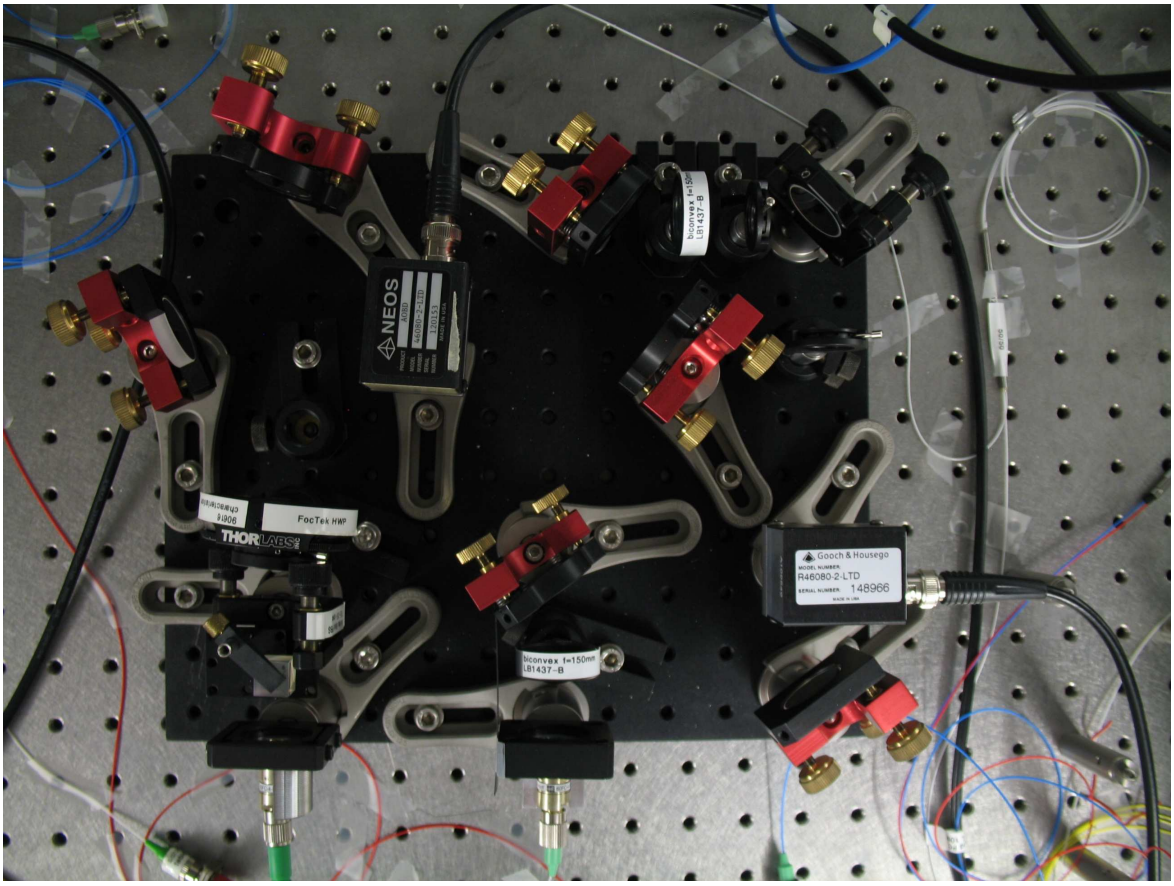

Figure C.1: Picture of the optical setup for producing pulses in the lab.

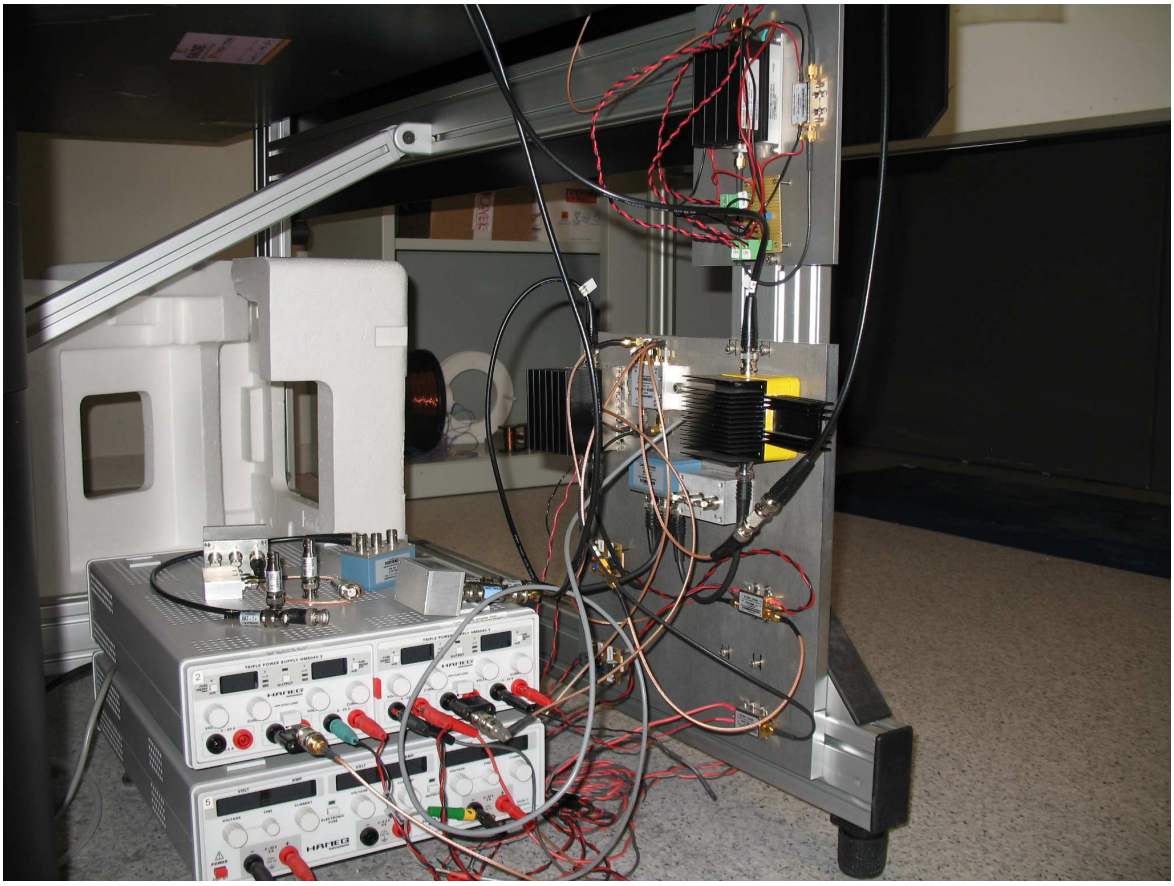

Figure C.2: Picture of the electronic setup for driving the AOMs. It is not show the arbitrary waveform generator.

List of abbreviations

AOM(s)	Acousto-optic modulator(s)
AWG	Arbitrary wave generator
B	Beam blocker
BS	Beam splitter
CW	continuous-wave
FADOF	Faraday anomalous dispersion optical filter
FC	Fiber Coupling
HWP	Half-wave plate
ICFO	Instituto de Ciencias Fotónicas
L	Lens
M	Mirror
NEP	Noise equivalent power
OPO	Optical parametric oscillator
PBS	Polarizing beam splitter
PD	Photodiode
PPKTP	Periodically-poled potassium titanyl phosphate
PSD(s)	Power spectral density(ies)
PZT	Piezoelectric transducer
RF	Radio-frequency
TTL	Transistor-Transistor Logic
VCO	Voltage controlled oscillator

List of Figures

Acknowledgments

Moral thanks

To my wife Anaid Rosas Navarro; to my parents and brothers (Miguel de Icaza, Mariblanca Astiz, Francisco Isaac, Aitor Lander, Iker Loic, Lartaun Aramis, Miguel, Pilar); to my brother-friends Roberto León, Jiri Svozilik, Rafael Betancur, Gianvito Lucivero, Isaac Ortigoza, Leonid Serkin, Xuan Loc, Alvaro Martínez Ramirez, Palestina Luz Llamas, Faviola Llamas, Heinrich Terborg, Atahualpa Solorzano Kraemer, Nigel Robinson, Ioan Stan, Ernesto Alvarez, Hiram Hernández, Edna Hernandez González; to the gurus Juan Carlos Arredondo, José Gabriel Aguirre, Victor Manuel Velazquez, Enrique López Moreno, Rafael Barrio, Mario Napolitano, René Asomoza Palacio, María Elena Navarro, Luciana Astiz and Ronan Le Bras.

Scientific thanks

First, I want to thank the other hand that was working with me in the lab, I want to thank my lab mate Vito Giovanni Lucivero, who was an essential element for getting the job done, through his help in the lab, helping me in acquiring the data, discussing and analyzing, also more important than all the other contributions, for his encouragement and friendship. Secondly, the head of our team, to my advisor Morgan W. Mitchell for all his help with the theory and his guidance. Morgan is truly an exceptional scientist that contributed strongly to my scientific training, not always in the way I wanted,

since my thinking is always more intuitive than deductive, and his is the opposite. And therefore, I have learned a lot from him in my stay at ICFO. Thirdly, my office mates Florian Wolfgramm, Brice Dubost and Ferran Martín Ciurana, with whom I discussed several ideas of the present document, and their critical point of view lead to several improvements. Fourthly to Roberto León Montiel that guide me in programming using Matlab and also helping to improve the quality of the present document. Fifthly, to Xavier Menino Pizarro and his team in the mechanical workshop, for making the custom mechanical pieces, together with José Carlos Cifuentes González and his team in the electronical workshop, for giving advice for the electronics and for making custom pieces. Next, to the gurus: Mario Napolitano, Ana Predojević and Matteo Cristiani, whom were guides in the first steps of the design of the experiment. To my lab mates Federica Beduini and Joanna Zielińska, who were there for commenting each time that was needed, including the group meetings with our boss. Following by, the rest of the group, who gave me valuable comments: Naeimeh Behbood, Giorgio Colangelo, Robert Sewell, Silvana Palacios Álvarez, Natali Martínez de Escobar, Thomas Vanderbruggen and Simon Coop.

Of course, I want to thank deeply the leader of ICFO: Lluis Torner, who has the vision and the spirit to create the Institute of Photonic Sciences (ICFO), which was my home from October 2008, when I began my Master. Also I want to thank all his administration team that make our life easier in ICFO, they are a strong help.

I want to thank my Ph.D. thesis reviewers: Jordi Mompart, John Calsamiglia, Juan Pérez Torres, Verònica Ahufinger and Hugues de Riedmatten.

Scientist and engineers which help in one way or another: Alessandro Cère, José Gabriel Aguirre, Anaid Rosas Navarro, Juan P. Torres, Jean-luc Doumont, Venkata Ramaiah Badarla, Jiri Svozilik, Jürgen Eschner, Jens Biegert, Turgut Durduran, Romain Quidant, Joel Villatoro, Pablo Loza Alvarez, Guillermo Alejandro Cardenas Sevilla, Marco Koskorrech, Ricardo Saiz, Jorge Luis Domínguez Juárez, Daniel Mitrani, Alejandra Valencia, Juan Manuel Fernández López, Marc Jofre Cruanyes, Alejandro Zamora, Osamu Takayama, Chirag Dhara,

Philipp Hauke, Xuan Loc, Xavier Délen, Alexander Dubrovkin, Elad Schleifer, David Wu, Diana Serrano, Giovanni Milione, Miguel Mireles, Alvaro Casas Bedoya, Dirk Fabian, Anna Krita, Armand Niederberger, Maria Serikova, Mena Issler, Priyanth Mehta, Sergei Slussarenko, and many others.

Funding

Personal Funding

This thesis and project was supported by the "Ministerio de Ciencia e Innovación" with the 4-year "Formación de Personal Investigador (FPI)" scholarship: BES-2009-017461, from the project FIS2007-60179.

Also, my Master studies (first academic year) were supported by a Master scholarship from the Institute of Photonic Science.

My last year was supported by the "Ministerio de Empleo y Seguridad Social" with the "Prestación Contributiva".

Research Funding

European Research Council project "AQUMET", the Spanish MINECO project "MAGO", FIS2011-23520, "Fundació Privada CELLEX Barcelona", Spanish MINECO project FIS2007-60179, and the Quantum Optical Information Technology (QOIT) project funded by the program CONSOLIDER-INGENIO 2010.

Bibliography

[1] Y. Painchaud, M. Poulin, M. Morin, and M. Tétu, "Performance of balanced detectionin a coherent receiver," Opt. Express **17**, 3659–3672 (2009).

[2] H.-G. Bach, "Ultra-broadband photodiodes and balanced detectors towards 100 gbit/s and beyond," in "Proc. SPIE," , vol. 6014 (2005), vol. 6014, pp. 60,140B–60,140B–13.

[3] R. Loudon and P. Knight, "Squeezed light," Journal of Modern Optics **34**, 709–759 (1987).

[4] K. Banaszek and K. Wódkiewicz, "Operational theory of homodyne detection," Phys. Rev. A **55**, 3117–3123 (1997).

[5] T. C. Zhang, J. X. Zhang, C. D. Xie, and K. C. Peng, "How does an imperfect system affect the measurement of squeezing?" Acta Physica Sinica-overseas Edition **7**, 340–347 (1998).

[6] A. Predojević, Z. Zhai, J. M. Caballero, and M. W. Mitchell, "Rubidium resonant squeezed light from a diode-pumped optical-parametric oscillator," Phys. Rev. A **78**, 063,820– (2008).

[7] I. H. Agha, G. Messin, and P. Grangier, "Generation of pulsed and continuous-wave squeezed light with rb-87 vapor," Optics Express **18**, 4198–4205 (2010).

[8] S.-H. Youn, "Novel scheme of polarization-modulated ordinary homodyne detection for measuring the polarization state of a weak field," Journal of the Korean Physical Society **47**, 803–808 (2005).

[9] S.-H. Youn, *Measurement of the Polarization State of a Weak Signal Field by Homodyne Detection* (InTech, available from: http://www.intechopen.com/books/photodetectors/, from the book [65], 2012), chap. 17, pp. 389–404.

[10] M. Kubasik, M. Koschorreck, M. Napolitano, S. R. de Echaniz, H. Crepaz, J. Eschner, E. S. Polzik, and M. W. Mitchell, "Polarization-based light-atom quantum interface with an all-optical trap," Phys. Rev. A **79**, 043,815– (2009).

[11] D. Sheng, S. Li, N. Dural, and M. V. Romalis, "Subfemtotesla scalar atomic magnetometry using multipass cells," Phys. Rev. Lett. **110**, 160,802– (2013).

[12] D. Budker and M. Romalis, "Optical magnetometry," Nature Physics **3**, 227–234 (2007).

[13] F. Wolfgramm, A. Cerè;, F. A. Beduini, A. Predojević, M. Koschorreck, and M. W. Mitchell, "Squeezed-light optical magnetometry," Phys. Rev. Lett. **105**, 053,601– (2010).

[14] V. G. Lucivero, P. Anielski, W. Gawlik, and M. W. Mitchell, "Shot-noise-limited magnetometer with sub-pt sensitivity at room temperature," arXiv **quant-ph**, 1403.7796v2 (2014).

[15] M. Koschorreck, M. Napolitano, B. Dubost, and M. W. Mitchell, "Sub-projection-noise sensitivity in broadband atomic magnetometry," Phys. Rev. Lett. **104**, 093,602– (2010).

[16] N. Behbood, F. M. Ciurana, G. Colangelo, M. Napolitano, M. W. Mitchell, and R. J. Sewell, "Real-time vector field tracking with a cold-atom magnetometer," Applied physics letters **102**, 173,504– (2013).

[17] H. Hansen, T. Aichele, C. Hettich, P. Lodahl, A. I. Lvovsky, J. Mlynek, and S. Schiller, "Ultrasensitive pulsed, balanced homodyne detector: application to time-domain quantum measurements," Opt. Lett. **26**, 1714–1716 (2001).

[18] Y. Chen, D. M. de Bruin, C. Kerbage, and J. F. de Boer, "Spectrally balanced detection for optical frequency domain imaging," Opt. Express **15**, 16,390–16,399 (2007).

[19] P. J. Windpassinger, M. Kubasik, M. Koschorreck, A. Boisen, N. Kjæ rgaard, E. S. Polzik, and J. H. Müller, "Ultra low-noise differential ac-coupled photodetector for sensitive pulse detection applications," Measurement Science and Technology **20**, 055,301 (2009).

[20] V. Ruilova-Zavgorodniy, D. Y. Parashchuk, and I. Gvozdkova, "Highly sensitive pump–probe polarimetry: Measurements of polarization rotation, ellipticity, and depolarization," Instruments and Experimental Techniques **46**, 818–823 (2003).

[21] S. V. Vaseghi, *Advanced Digital Signal Processing and Noise Reduction* (John Wiley & Sons Ltd, 2000).

[22] I. K. Kominis, T. W. Kornack, J. C. Allred, and M. V. Romalis, "A subfemtotesla multichannel atomic magnetometer," Nature **422**, 596–599 (2003).

[23] I. M. Savukov, S. J. Seltzer, M. V. Romalis, and K. L. Sauer, "Tunable atomic magnetometer for detection of radio-frequency magnetic fields," Phys. Rev. Lett. **95**, 063,004– (2005).

[24] R. P. Abel, U. Krohn, P. Siddons, I. G. Hughes, and C. S. Adams, "Faraday dichroic beam splitter for raman light using an isotopically pure alkali-metal-vapor cell," Opt. Lett. **34**, 3071–3073 (2009).

[25] F. Wolfgramm, Y. A. de Icaza Astiz, F. A. Beduini, A. Cerè, and M. W. Mitchell, "Atom-resonant heralded single photons by interaction-free measurement," Phys. Rev. Lett. **106**, 053,602– (2011).

[26] J. A. Zielińska, F. A. Beduini, N. Godbout, and M. W. Mitchell, "Ultranarrow faraday rotation filter at the rb d_1 line," Opt. Lett. **37**, 524–526 (2012).

[27] Y. Wang, X. Zhang, D. Wang, Z. Tao, W. Zhuang, and J. Chen, "Cs faraday optical filter with a single transmission peak resonant with the atomic transition at 455 nm," Opt. Express **20**, 25,817–25,825 (2012).

[28] Y. A. de Icaza Astiz, V. G. Lucivero, R. d. J. Len-Montiel, and M. W. Mitchell, "Optimal signal recovery for pulsed balanced detection," Phys. Rev. A **90**, 033,814– (2014).

[29] Y. A. de Icaza Astiz, "Binary coherent beam combining with semiconductor tapered amplifiers at 795 nm," Master's thesis, Msc in Photonics. UPC Barcelona Tech (2009).

[30] F. A. Beduini, N. Behbood, Y. de Icaza, B. Dubost, M. Koschorreck, M. Napolitano, A. Predojević, R. Sewell, F. Wolfgramm, and M. W. Mitchell, "Quantum metrology with atoms and photons," Opt. Pura Apl. **44**, (2) 315–323 (2011).

[31] F. A. Beduini, J. A. Zielińska, V. G. Lucivero, Y. A. de Icaza Astiz, and M. W. Mitchell, "Interferometric measurement of the biphoton wave function," Phys. Rev. Lett. **113**, 183,602 (2014).

[32] F. A. Beduini, J. A. Zielińska, V. G. Lucivero, Y. A. de Icaza Astiz, and M. W. Mitchell, "A macroscopic quantum state analysed particle by particle," arXiv **quant-ph**, 1410.7079v1 (2014).

[33] H.-A. Bachor and T. C. Ralph, *A Guide to Experiments in Quantum Optics* (Wiley-VCH, 2004).

[34] D. J. McCarron, "A guide to acousto-optic modulators," Tech. rep., Durham University (2007).

[35] R. Paschotta, *Encyclopedia of Laser Physics and Technology* (Wiley-VCH, 2008).

[36] United-Crystals, "Tellurium dioxide (teo2)," Tech. rep., United Crystals, available at http://www.unitedcrystals.com/ (2013).

[37] Gooch and Housego, "46080-1-ltd," Tech. rep., Gooch and Housego (2013).

[38] R. G. Driggers, ed., *Encyclopedia of Optical Engineering* (Marcel Dekker, 2003).

[39] Thorlabs, *Operation Manual Thorlabs Instrumentation PDB100 Series Balanced Amplified Photodetectors PDB150* (2007).

[40] T. Ezaki, G. Suzuki, K. Konno, O. Matsushima, Y. Mizukane, D. Navarro, M. Miyake, N. Sadachika, H.-J. Mattausch, and M. Miura-Mattausch, "Physics-based photodiode model enabling consistent opto-electronic circuit simulation," in "Electron Devices Meeting, 2006. IEDM '06. International," (2006), pp. 1–4.

[41] Hamamatsu Photonics K. K., *Opto-semiconductor handbook — Chapter 2: Si photodiodes* (Hamamatsu, available from: https://www.hamamatsu.com/sp/ssd/doc_en.html, 2012), chap. 2, pp. 22–66.

[42] B. E. A. Saleh and M. C. Teich, *Fundamentals of Photonics* (Wiley, 2007), 2nd ed.

[43] G. Heinzel, A. Rüdiger, and R. Schilling, "Spectrum and spectral density estimation by the discrete fourier transform (dft), including a comprehensive list of window functions and some new flat-top windows," Tech. rep., Max-Planck-Institut für Gravitationsphysik (2002).

[44] R. Losada, "Periodogram psd using periodogram," Tech. rep., Mathworks (2007).

[45] R. Losada, "Pwelch power spectral density estimate via welch's method." Tech. rep., Mathworks (2007).

[46] K. Jacobs, *Stochastic Processes for Physicists* (Cambridge University Press, 2010).

[47] A. Predojević, "Rubidium resonant squeezed light from a diode-pumped optical-parametric oscillator," Ph.D. thesis, ICFO-UPC (2009).

[48] Toptica, *Manual DL 100* (2008).

[49] D. A. Steck, "Rubidium 87 d line data," Tech. rep., Oregon Center for Optics and Department of Physics, University of Oregon (2010).

[50] I. H. Agha, C. Giarmatzi, Q. Glorieux, T. Coudreau, P. Grangier, and G. Messin, "Time-resolved detection of relative-intensity

squeezed nanosecond pulses in an 87 rb vapor," New Journal of Physics **13**, 043,030 (2011).

[51] Rohde and Schwarz, *Operating Manual Spectrum Analyzer R&S FSL6* (2009).

[52] R. A. Chipman, *Polarimetry* (McGraw-Hill, Inc., from the book [66], 1995), vol. 2, chap. 22, pp. 22.21–22.37.

[53] H. Tompkins and E. A. Irene, eds., *Handbook of ellipsometry* (William Andrew, 2005).

[54] G. G. Stokes, *Mathematical and Physical Papers*, vol. 3 (Cambridge University Press, 2009).

[55] D. H. Goldstein and E. Collett, *Polarized light* (Marcel Dekker, Inc., 2003).

[56] R. M. A. Azzam, "Instrument matrix of the four-detector photopolarimeter: physical meaning of its rows and columns and constraints on its elements," J. Opt. Soc. Am. A **7**, 87–91 (1990).

[57] B. A. Robson, *The Theory of Polarization Phenomena* (Clarendon Press, Oxford, UK, 1974).

[58] A. Luis and L. L. Sánchez-Soto, "Phase-difference operator," Phys. Rev. A **48**, 4702–4708 (1993).

[59] L. Sánchez-Soto and A. Luis, "Quantum stokes parameters and phase difference operator," Optics Communications **105**, 84–88 (1994).

[60] N. Korolkova, G. Leuchs, R. Loudon, T. C. Ralph, and C. Silberhorn, "Polarization squeezing and continuous-variable polarization entanglement," Phys. Rev. A **65**, 052,306– (2002).

[61] J. Heersink, T. Gaber, S. Lorenz, O. Glockl, N. Korolkova, and G. Leuchs, "Polarization squeezing of intense pulses with a fiber-optic sagnac interferometer," Physical Review A **68**, 013,815 (2003).

[62] J. Heersink, V. Josse, G. Leuchs, and U. L. Andersen, "Efficient polarization squeezing in optical fibers," Opt. Lett. **30**, 1192–1194 (2005).

[63] R. J. Sewell, M. Koschorreck, M. Napolitano, B. Dubost, N. Behbood, and M. W. Mitchell, "Magnetic sensitivity beyond the projection noise limit by spin squeezing," Phys. Rev. Lett. **109**, 253,605 (2012).

[64] S. M. Tan, "Linear systems, available at http://home.comcast.net/~szemengtan/," Tech. rep., The University of Auckland (2013).

[65] S. Gateva, *Photodetectors* (InTech, available from: http://www.intechopen.com/books/photodetectors/, 2012).

[66] M. Bass, ed., *Handbook of optics* (McGraw-Hill, 1995).